Computers and Geotechnics. Submitted Nov 2022; Published Apr 2023.
https://doi.org/10.1016/j.compgeo.2023.105455

MPM-Based Mechanism And Runout Analysis Of A Compound Reactivated Landslide

Kun He[1*], Chuanjie Xi[1], Bo Liu[1], Xiewen Hu[1,2*], Gang Luo[1], Guotao Ma[3], Ruichen Zhou[1]

1. Southwest Jiaotong University, Faculty of Geosciences and Environmental Engineering, Chengdu, China
2. Southwest Jiaotong University, Engineering Laboratory Combined with National and Local of Spatial Information Technology of High-Speed Railway Operation Safety, Chengdu, China
3. University of Warwick, School of Engineering, Coventry, UK

Abstract Understanding the entire process of hydraulic-related landslide reactivations is crucial for risk assessment, which includes initiation and runout evolves from a small-deformation in the pre-failure stage to large-deformation after failure, with complex interactions between the materials in solid and liquid phases. This paper reproduces the entire process of a reactivated landslide using Material Point Method (MPM). The accuracy of MPM is validated in comparison to Limit Equilibrium Method (LEM) and Finite Element Method (FEM). The effects of antecedent rainfall and pre-existing groundwater on landslide runout and the deposits morphology are discussed. Results show that the antecedent rainwater rises the groundwater level and saturates the front edge of slope where the initial failure occurred. Three computed spatio-temporal distributions of pore water pressure show good agreement and match well with field evidence. The kinematic characteristics show that the landslide has different moving features with different microtopography, which reveals retrogressive failure in front and middle part of slope initially and compound retro- and pro-gressive failures occur at the rear edge. The results of unsaturated two-phase MPM are in better agreement with the measured morphology than full-saturated MPM. The antecedent rainfall and the pre-existing groundwater are the main contributing factors to the landslide runout.

Author Keywords: Landslide, Material point method, Pre-failure, Post-failure, Hydraulic-related

Computers and Geotechnics. Submitted Nov 2022; Published Apr 2023.
https://doi.org/10.1016/j.compgeo.2023.105455

Introduction

Ancient landslide deposits (ALD) are ubiquitous in tectonically active regions and are prone to sliding repeatedly influenced by external triggering factors (Gariano and Guzzetti 2016; Tang et al. 2019; Peranić et al. 2021). Due to the unconsolidated nature of ALD, hydraulic-related reactivated landslides have recently become more frequent. Landslides reactivated by rainwater infiltration and associated groundwater seepage are dangerous due to the long runout distance and flowing movement (Bertolini and Pizziolo 2008; Notti et al. 2021). Haque et al. (2019) reported 3876 rainfall-triggered landslides from 1995 to 2014 and found that the number of fatal landslides increased during this 20-year period, resulting in more than 150 thousands fatalities and 170 thousands casualties. Therefore, understanding the landslide initiation mechanism and the kinematic characteristics of the runout is crucial for assessing the risk of landslides related to hydraulic-related landslide risk assessment.

Great efforts have been conducted throughout the years to explore the initiation mechanisms, that is, the process from pre-failure to failure of hydraulic-related landslides (Zhang et al. 2021; Jiang et al. 2022; He et al. 2022). Importantly, rainfall and groundwater seepage are main factors induced the reactivation of ALD, and the dynamic response of ALD to the dominant rainfall process inducing their failures is essential for the reactivated modes (Peruccacci et al. 2017; Ma et al. 2021; Darrow et al. 2022). Compared with the normal rainfall-induced landslides, the materials and structures of the ALD are more complex, presenting the rock-soil mixture characteristic of assorted sizes and have special engineering mechanical properties (Luo et al. 2017; Cui et al. 2021; Chen et al. 2022). Influenced by hydraulic seepage deformation, the ALD have typical stress-seepage damage coupling characteristics. Therefore, the initiation mechanisms often involve complex interaction between the soild skeleton (rock-soil) and the liquid (interstitial pore water). Several classical methods were posed to deal with the slope stability caused by hydrodynamic influences, for instance, the uncoupled seepage Finite Element Method (FEM) with Limit Equilibrium Method (LEM), consists of non-deformation seepage analysis and Factor of Stability (*Fs*) computation (Janbu 1954; Bishop 1955; Morgenstern and Price 1965). However, solid deformation is not assessed into slope by this method, resulting in limitations for complex slope initiation mechanism analysis. An alternative method is the hydro-mechanical coupled FEM, which is formulated within the framework of continuum mechanics, can acquire the stress-strain information in respect to gravity and external forces, and can compute the seepage variations with hydraulic boundary conditions (Biot 1941; Borja et al. 2012; Kim et al. 2018). Soil deformations have been considered as small before slope failures, hence the traditional methods of LEM and FEM have been applied for past several decades (François et al. 2007; Masoudian et al. 2019; Jamalinia et al. 2020; Scaringi and Loche 2022).

The landslide runout process after slope failure occurred is crucial for risk management and the mechanics of the process is challenging because of its complexities. The post-failure behaviors are often associated with large deformations which differ from the pre-failure small deformations. The above traditional methods are not well suited for large-deformation analysis due to the resultant extreme mesh distortion. To this end, an appropriate numerical approach for large-deformation issues is indispensable. Advanced methods (Soga et al. 2016; He et al. 2018) have been posed including Smooth Particle Hydrodynamics (SPH), Discrete Element Method (DEM), Particle Flow Code (PFC), Particle Finite Element Method (PFEM), Numerical Manifold Method (NMM), Discontinuous Deformation Analysis (DDA) and Material Point Method (MPM) (Sulsky et al. 1994). Among them, the MPM has been improved and successfully applied into various fields, particularly in solving multiphase interaction problem in geotechnical community (Yerro et al. 2015; Soga et al. 2016; Liang and Zhao 2019; Cuomo et al. 2021a; Ceccato et al. 2021; Li et al. 2021; Nguyen et al. 2022). MPM can simulate the hydro-mechanical coupled behaviors during a landslide. Previous MPM-derived studies examine the post-failure of saturated/unsaturated slope by imposing the critical phreatic surface instead of rainwater infiltration process (Soga et al. 2016; Lei et al. 2020). Bandara et al. (2016) introduced a flux boundary in MPM for rainfall infiltration using a full-coupled hydro-mechanical formulation for both saturated and unsaturated soils. Feng et al. (2021) developed a two-layer hydro-mechanical coupled MPM for performing soil-water interaction in unsaturated soils and analyzed rainfall-induced landslide. Cuomo et al. (2021b) employed the formulation considering an antecedent rainfall process preceding the 1995 Fei Tsui Road landslide and outlined the influence of the initial suction on time, type, and runout of the landslide. Although in the real case the failure occurred due to a joint effect of rainwater infiltration and exfiltration of groundwater, it is true that the initial suction value at the beginning of infiltration being set as constant along the depth has contributed to the simulation of complex hydraulic-related landslide, the realistic groundwater table with heterogeneities was simplified. Referring to the presence of groundwater in the area affected by the landslide, few studies have addressed the initial groundwater condition influencing the landslide behaviors.

Most of the numerical simulations allow the separate computation of pre-failure and post-failure stages of hydraulic-related landslide (Chen et al. 2021; Xu et al. 2022; Su et al. 2022). The entire landslide process include the small deformations in the pre-failure stage and large deformations during the runout, and then returns to small deformations during deposition stage. The accurate and smooth reproduction of the entire landslide process is still a challenging work. Moreover, the initiation mechanisms and runout behaviors depend on original slope geometry, which means complex-shaped slopes have compound and complex initiation and kinematic characteristics. Relatively few MPM-based studies investigate the compound pre-failure and post-failure of hydraulic-related landslide.

This paper uses MPM to analyze the initiation mechanism response to the antecedent rainfall and pre-existing groundwater table and to examine the runout behaviors of a given reactivated landslide. The specific objectives are: 1) to explore the pre-failure deformations of landslide, especially for the variation in porewater pressure (PWP) during the rainfall process; 2) to investigate the post-failure process, kinematic characteristics, and strain-seepage changes during landslide; 3) to evaluate the applicability of MPM in solving two-phase seepage and small deformation problems compared with classical methods; 4) to study the effect of the presence or absence of antecedent rainfall and pre-existing groundwater on the landslide runout distance and deposition. The results have potential to provide insights into the entire landslide process for such hydraulic-related landslides.

Methods

We conduct the MPM analysis from pre-failure (initiation) to post-failure (runout and deposition) for a compound landslide in an unsaturated slope. The pre-failure multi-field variations are compared to the classical LEM and FEM-based results to validate the capability of MPM on simulating from small- to large-deformation. The MPM code employed in the study is from Anura3D MPM Community (Anura3D 2022), which is an efficient tool for solving large deformation problems in geotechnics. The predominant feature of MPM is that a continuum medium is schematized to a combination of material points (MPs) and background mesh. The discreted MPs can freely move through the problem domain based on the Lagrangian description of the media, and can carry all the physical information and stress-strain field values. The information of MPs are then transmitted to the background mesh. The governing equations of background mesh nodes are then solved in an incremental scheme at each time step. By synthesizing the advantages of Lagrangian particles and Eulerian mesh, the interference of convective terms or mesh distortion in solving large deformation problems is prevented. Nowadays, many variations of original algorithm have been proposed, tailored for a wide range of multidisciplinary applications (Jiang et al. 2016; Yerro et al. 2016; de Vaucorbeil et al. 2020; Kohler and Puzrin 2022). Recently, the MPM has been successfully conducted to model hydraulic-related landslides (Wang et al. 2018; Liu and Wang 2021; Yerro et al. 2022). Compared to more universe three phases formulations, Ceccato et al. (2019) indicate that in numerous natural cases of landslides the differences between two phases and three phases formulations are negligible. Thus, the medium comprised of two phases (solid and liquid) for both saturated and unsaturated sliding materials is often applied. This study uses coupled hydro-mechanical two-phase single-point MP to

Computers and Geotechnics. Submitted Nov 2022; Published Apr 2023.
https://doi.org/10.1016/j.compgeo.2023.105455

simulate the PWP variations of a reactivated landslide. The effects of partial saturation in soil response are considered. Detailed basic mathematical formulations of MPM can be found in Ceccato et al. (2021).

Computational procedure

Firstly, the information is mapped from the MPs to the computational nodes by means of interpolation functions at the beginning of each time step (Fig. 1a). Then the governing equilibrium equations of mass and momentum conservation are solved (Fig. 1b) and the information (velocity, position) at the MPs are updated through the nodal values, which are used to compute the stresses and strains (Fig. 1c). Finally, the deformed background mesh is subsequently reset to avoid the excessive mesh distortion and ready for the next computational cycle (Fig. 1d).

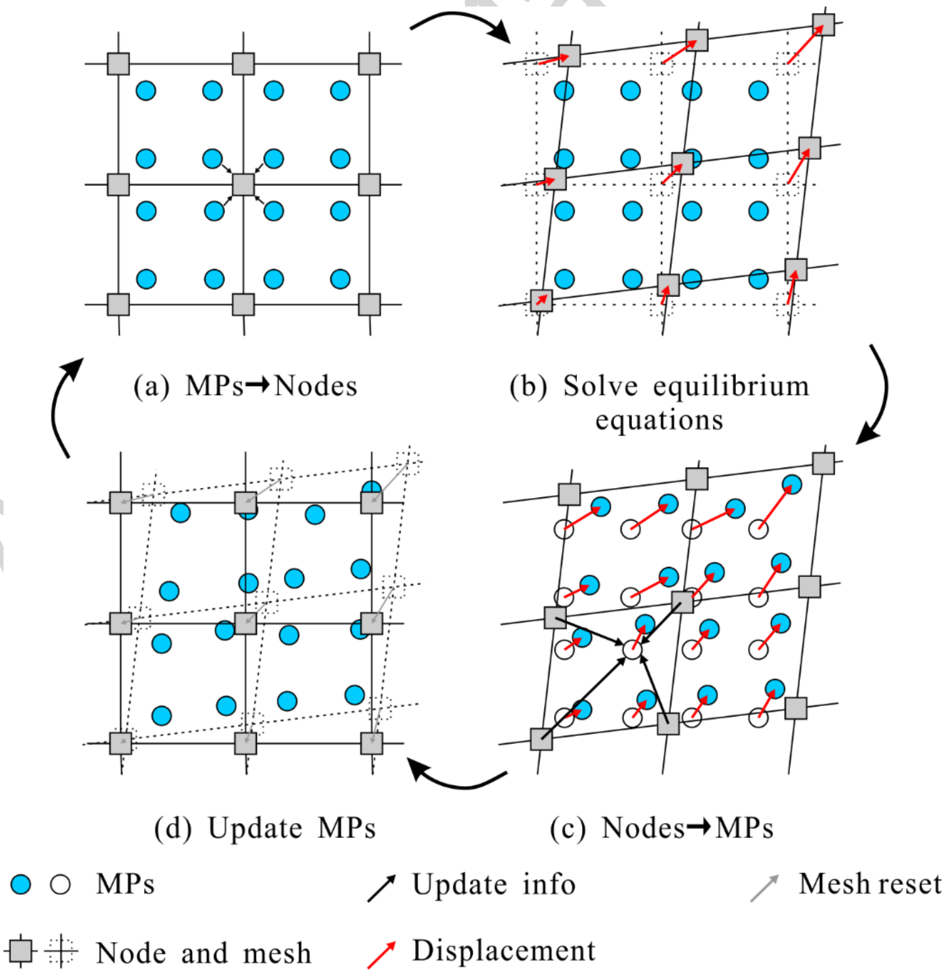

Fig. 1 Computational scheme of MPM

Case study

The Boli reactivated landslide occurred in Yanyuan County of Sichuan China (Fig. 2), after continous rainfall of 5th to 18th July 2018 (Fig. 4). A cumulative precipitation of 350.6 mm was recorded in this period. The landslide area had a length of about 1360 m and a maximum width of 810 m and a height difference of 310 m. The landslide covered 59.2× 10^4 m^2 and the deposition volume was estimated to be 1390.6 × 10^4 m^3 (He et al. 2021). Field investigations outlined that the landslide occurred in ALD and tensile cracks appeared in the front edge since 13rd July. This landslide destroyed 186 houses and dammed the Taozi gully at the toe.

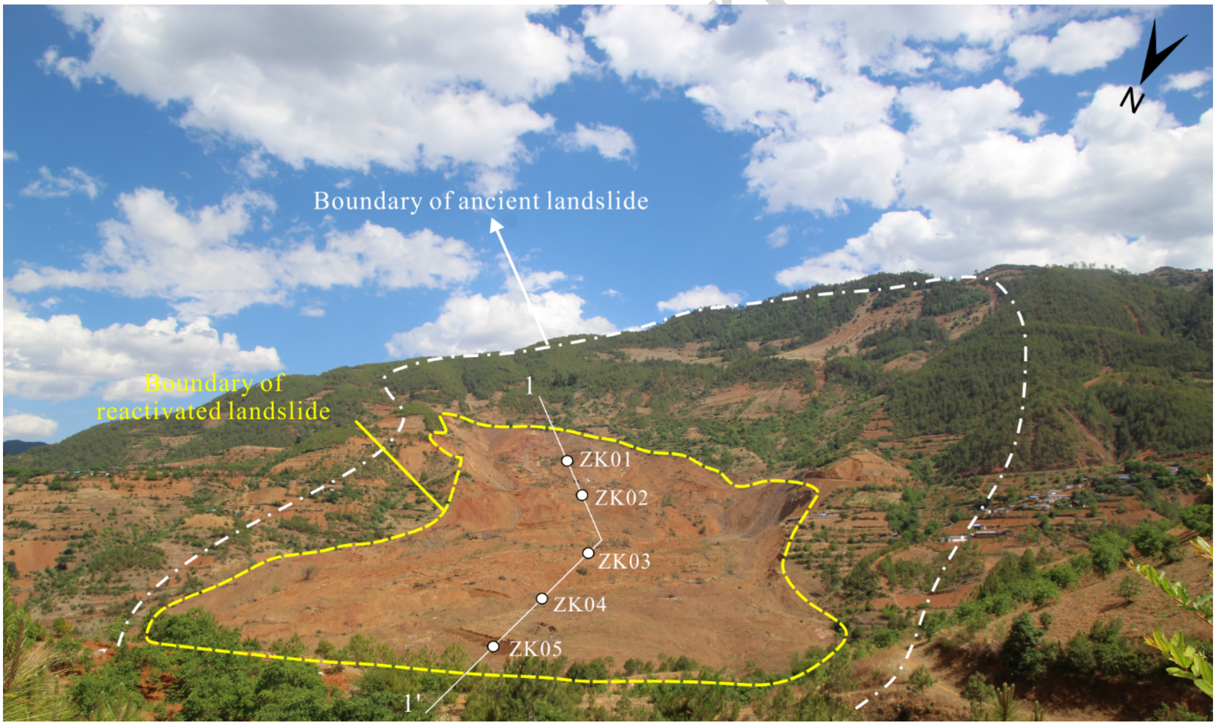

Fig. 2 Reactivated landslide overview

Information on sliding soils and groundwater along the slope was derived from in situ and laboratory tests. Fig. 3 shows the distribution of boreholes along the main profile of the slope. The

Computers and Geotechnics. Submitted Nov 2022; Published Apr 2023.
https://doi.org/10.1016/j.compgeo.2023.105455

depth of ALD vary from 3 to 50 m obtained by borehole drilling. The deposits consist of two layers of different materials, with silty clay at the upper part, containing clay particles with high viscosity and presenting a thickness of approximately 3~10 m. While the lower layer belongs to argillaceous gravels, which has a thickness of about 5~50 m. The dual structure of slope soils is formed due to the differential weathering of ALD. The sliding surface follows the interface of bedrock and ALD. The boreholes revealed the groundwater level under natural conditions, which was 10~20 m below the ground surface. Fig. 4 shows the daily rainfall from 5 to 18 July, 2018, with a cumulative rainfall of 350.6 mm and a maximum daily rainfall of 69.4 mm on 13 July. The landslide occurred on 19 July, 2018, which had no precipitation.

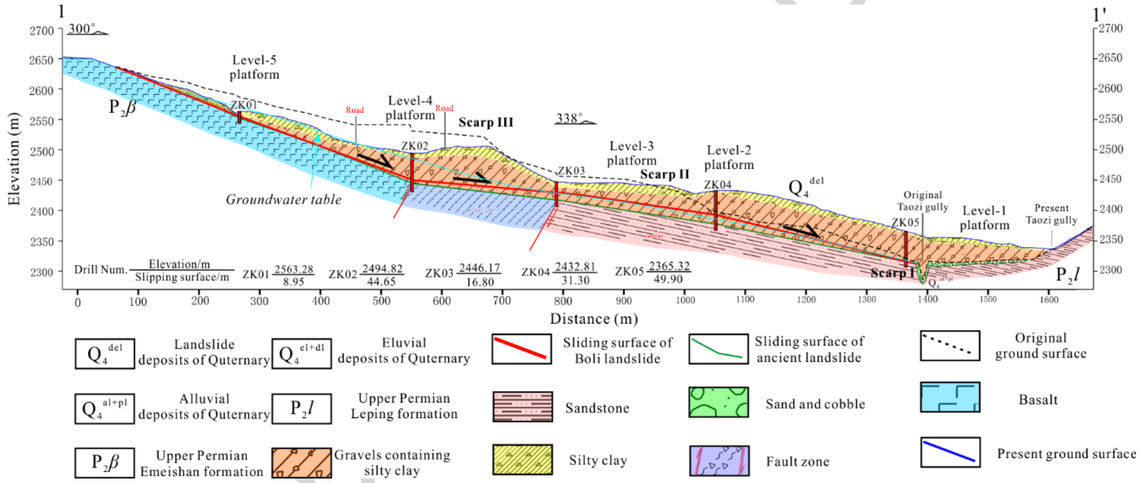

Fig. 3 Geological profile of the reactivated landslide: longitudinal profile 1-1' in Fig. 2

https://doi.org/10.1016/j.compgeo.2023.105455

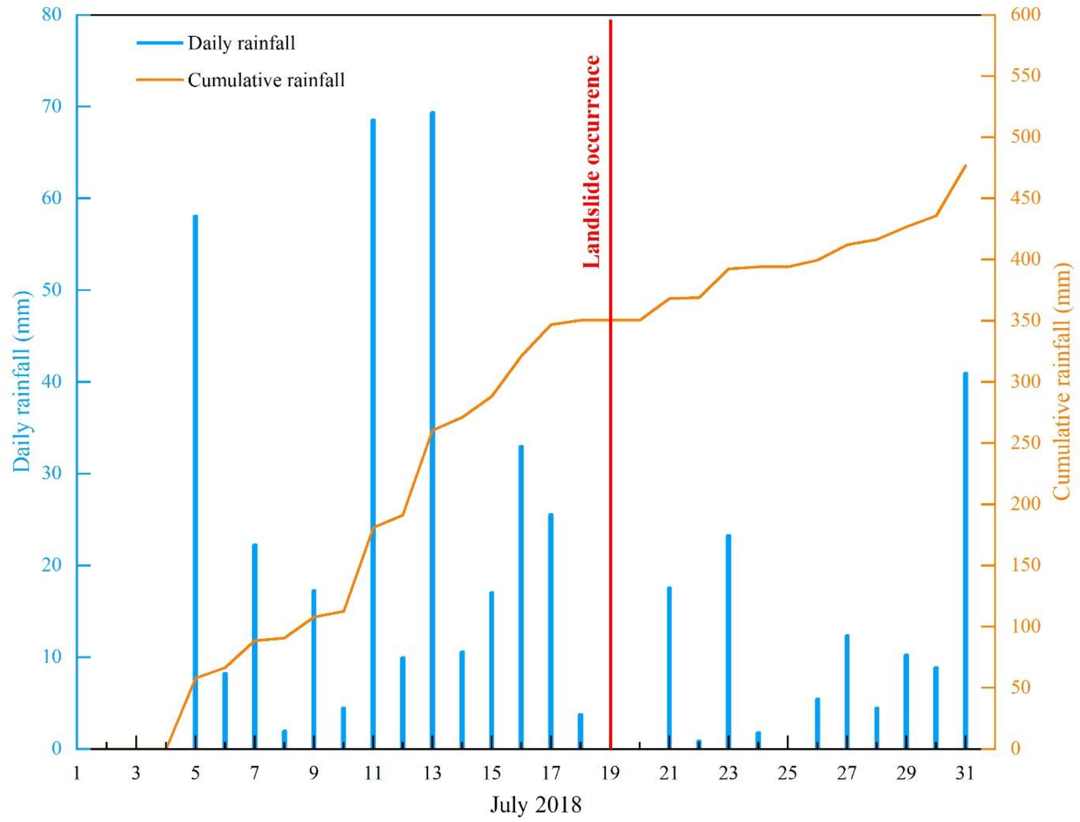

Fig. 4 Daily and cumulative rainfall in the landslide area for July 2018. Antecedent rainfall occurred on July 5–18. Rainfall data is derived from the rainfall station

MPM model setup and parameters

The numerical calculation model is established based on the geological profile in Fig. 5, with the X axis as the horizontal direction and the Y axis as the vertical direction. The calculation model is set at 1:1, with the horizontal length of 1700 m and the vertical height of 385 m. GiD 14.0 software (GiD 2018) was used to conduct model setup. Fig. 5 shows the MPM model and monitoring points of the slope. Since the sliding zone is relatively thin in thickness (10~20 cm), the defined contact surface was selected to establish the sliding surface, where a frictional contact algorithm is implemented. Silding mass adopts Mohr-Coulomb model and bedrock adopts linear elastic model. A three-node linear triangular element with 6 MPs was designed for the soil element. The size of the background mesh of the sliding mass was 2m×2m, and the size of the background mesh of other parts was 10m×10m. In

https://doi.org/10.1016/j.compgeo.2023.105455

order to reduce the number of material points, since no deformation was observed within the bedrock, the corresponding background meshes were discretized into 1 material point for each element. In total, the MPM model consisted of 48132 elements, 244452 MPs (240072 MPs for sliding mass and 4380 MPs for bedrock), and 24256 nodes. Six monitoring points were distributed at the surface of the sliding mass and four monitoring points were assigned to the bottom of sliding mass to investigate the variations in velocity, displacement, pore water pressure, and stress-strain during the pre- and post-failure of the landslide.

The bottom of the model background grid was fixed in the XY direction for solid phase and in the Y direction for liquid phase, the left boundary was fixed in the X direction for solid phase and the boundary above the groundwater table was fixed in the X direction for liquid phase, the right boundary was fixed in X direction for both the solid and liquid phases, and the upper part was fixed in Y direction for both the solid and liquid phases. Since the reactivated landslide was induced by the combination of rainfall and groundwater, the effects of groundwater and rainfall were considered in the modeling. The groundwater level was determined by the borehole drilling and set as the initial condition of the model. The rainfall was the hyetograph of the recording station and set as the hydraulic boundary of the model, which was applied to the upper surface of the model (Fig. 5). The application of this infiltration boundary condition is based on a predictor-corrector scheme (Martinelli et al. 2020). MPM discretized the sliding mass involved in the failure into MPs. The background mesh was divided by Eulerian method to integrate the momentum equation and update the physical quantities.

Computers and Geotechnics. Submitted Nov 2022; Published Apr 2023.
https://doi.org/10.1016/j.compgeo.2023.105455

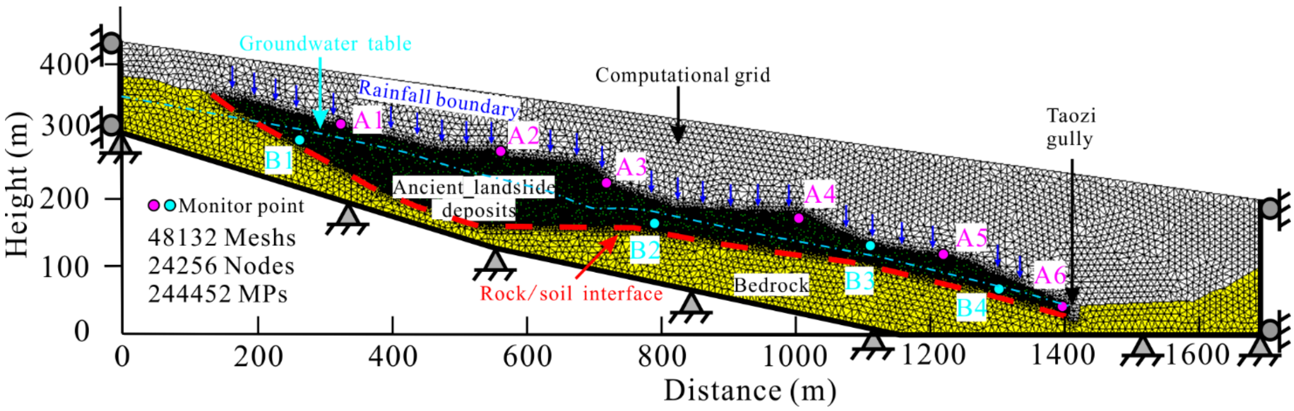

Fig. 5 Geometry and discretization of the MPM model

The MPM analysis is conducted to simulate the pre-failure, failure and post-failure behaviors through a unified calculation model. To do this, different time steps were defined during the landslide process: a) in the rainfall infiltration stage the time interval is assumed equal to 1 day, with the total time of 14 days. However, because the numerical scheme is explicit, the calculation is conditionally stable and the time step increments are very small. For this reason, in the first stage of infiltration, we performed time scaling to indirectly achieve the large time step computations by converting the day to second, thus, the total computation time was 14 s, and a time step of 5×10^{-3} s was applied. The typical values of the saturated hydraulic conductivity for ALD samples are at the order of magnitude of about 10^{-6} m/s. To match the simulation duration as well as to reduce the computational cost to an acceptable level, an accelerated seepage analysis is performed by adopting an increasing value of k_{sat}. The permeability of sliding mass was multiplied by 86400, which is equal to seconds in one day, that is, an increased k_{sat} value of 3.11×10^{-1} m/s is adopted. The infiltration rates were monitored by rainfall station with the scale of mm/day, then they were divided by 86400 and applied in the computation. While the b) subsequent runout stage was discretized in 5×10^{-3} s. The simulation was terminated until landslide motion stopped, which meant the velocity of the sliding mass was equal to zero. A damping factor defined as a force proportional to the corresponding unbalanced force, is also considered in the analysis (Kafaji 2013). In dynamic problems, where accelerations play an important role, the damping factor should be small in order to avoid overdamping but sufficiently large to reduce spurious oscillations. Values within the range of 0-5% are typically used (Jassim et al. 2013; Abe et al. 2014; Bandara and Soga 2015). Five calculations with different local damping ratio are proposed in order to investigate the effect of including local damping on the dynamic computation (Fig. S1, see supplementary material). A local damping coefficient for all active elements of 5% is applied for both the infiltration phase and during the runout, which also a unique value suggested by Yerro et al. (2019), to prevent the model from becoming overly damped during dynamic computation, which could result in high energy dissipation and could thus influence the accuracy of predictions of the kinematic behavior of landslides, such as underestimating the velocity and runout distance.

Tables 1 and 2 summarize the material parameters used in the simulation. The Mohr-Coulomb failure criterion with effective stress properties was adopted for ALD. Coupled hydro-mechanical simulation with two-phase single-point formulation was assigned to the ALD to perform analysis on the pore water pressure (PWP) changes, while the contact surface was tackled through the one phase single-point formulation. The ALD was defined as unsaturated. The physical-mechanical parameters were determined by in situ and laboratory tests, while the hydraulic parameters, including porosity, saturated water content, permeability coefficient were determined by drill hole pressure tests, consolidation tests. The soil-water characteristic curve was fitted by using van Genuchten model (van Genuchten 1980) (Fig. 6). The shear strength of contact surface was obtained from direct shear tests on sliding zone soils.

Computers and Geotechnics. Submitted Nov 2022; Published Apr 2023.
https://doi.org/10.1016/j.compgeo.2023.105455

Table 1 Input material parameters for MPM simulation

Parmeter	Unit	Pore water	ALD	Bedrock
Material type		/	Saturated-unsaturated	Dry
Constitutive model		/	Mohr-Coulomb	Linear elastic
Porosity, n	/	/	0.225	/
Unit weight, γ	kN/m^3	10	23.5	27.8
Cohesion, c	kPa	/	25.4	/
Friction angle, φ	°	/	17.2	/
Poisson's ratio, v	/	/	0.30	0.23
Elastic modulus, E	MPa	/	45	30000
Bulk modulus, K	MPa	200	/	/
Saturated permeability, k	m/s	/	3.6×10^{-6}	/
Dilation angle, ψ	°	/	0	/

Table 2 Parameters for contact surface

Parmeter	Value
Cohesion c, kPa	17.9
Friction angle φ, °	12.5

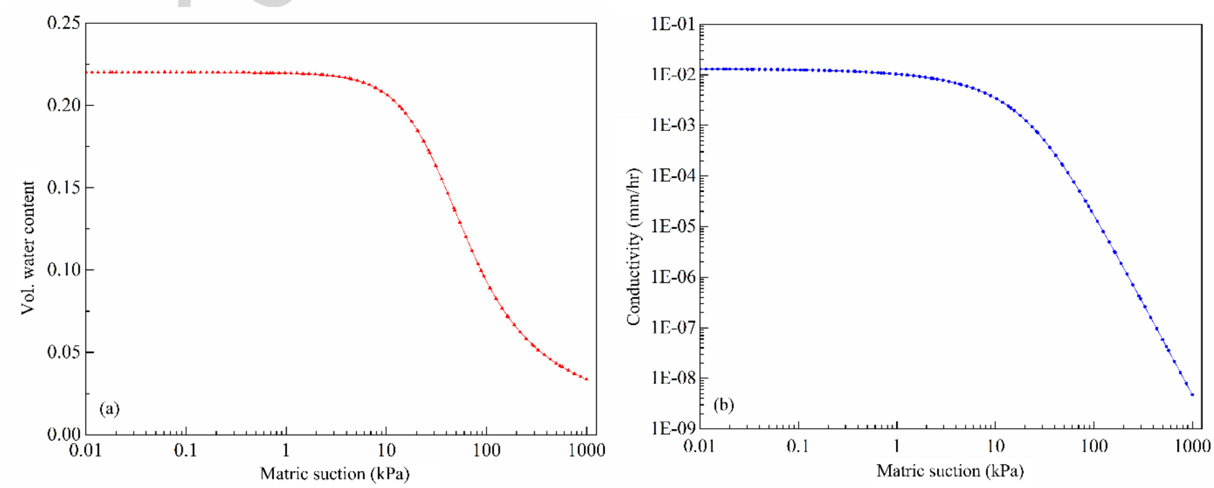

https://doi.org/10.1016/j.compgeo.2023.105455

Fig. 6 (a) Penetration function curve of the sliding mass; (b) Soil-water characteristics curve of the sliding mass

Results

Pre-failure behaviors

Fig. 7 shows the slope behavious correpsponding to the antecedent rainfall infirltration. Based on the seepage field simulation results (Fig. 7a), in the early stage of rainfall, the sliding soil presented the rapid infiltration, and the negative PWP of surface soils decreased constantly. Continuous precipitation saturated the soil and increased the bulk density of the soils. Due to the thickness of the sliding mass at the front edge was lower than that of the rear edge, and the infiltration path at the front edge was short, thus the front edge of the slide mass with relatively gentle terrain reached the saturated state initially. Then, the precipitation continued to infiltrate the sliding soils at the rear edge. When the front sliding soils reached saturated state, groundwater infiltrated by rainfall continuously accumulated on the potential sliding surface, increasing PWP on the sliding surface. Consequently, the soil suction decreased with the increasing of PWP, resulting in mean effective stress decreased (Fig. 7b). Fig. 7c depicts the development and distribution of the deviatoric strain of the slope at different time steps for the evaluation of the shear failure surface during the rainwater infiltration stage. The soil failed retrogressively from the lower to upper slope. At t = 5 day, the shear failure surface began to develop at the soil-bedrock interface at the bank slope of Taozi gully. Meanwhile, the maximum displacement was observed at the front edge (Fig. 7d). The deviatoric strain also began to present at the scarps along the slope profile and the rear edges. At t = 7 days, shear deformations could be more clearly observed at the bank slope and appeared to exhibit a rotational movement at the scarps. At the end of the rainfall infiltration stage, distinct shear surfaces were presented at the front edge, scarps and the rear edge, with maximum displacement reached about 1.5 m (Fig. 7d and Fig. 8).

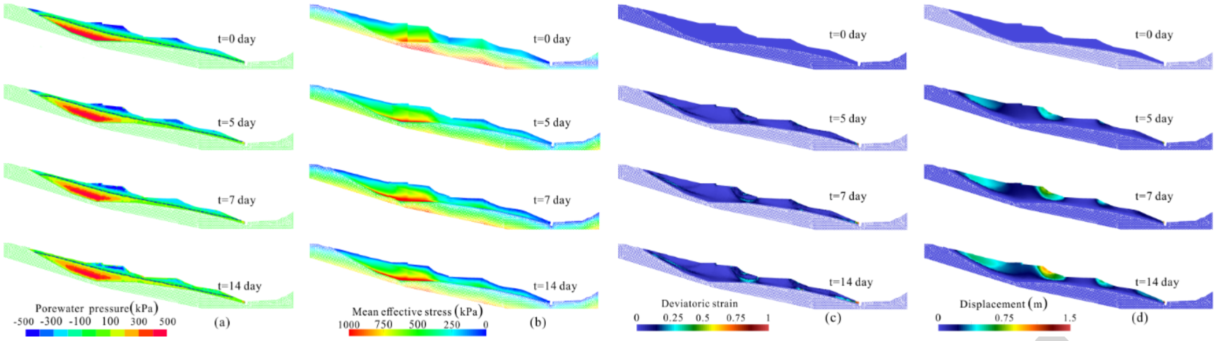

Fig. 7 Variation in (a) PWP, (b) mean effective stress, (c) deviatoric strain and (d) displacement computed in rainfall infiltration stage

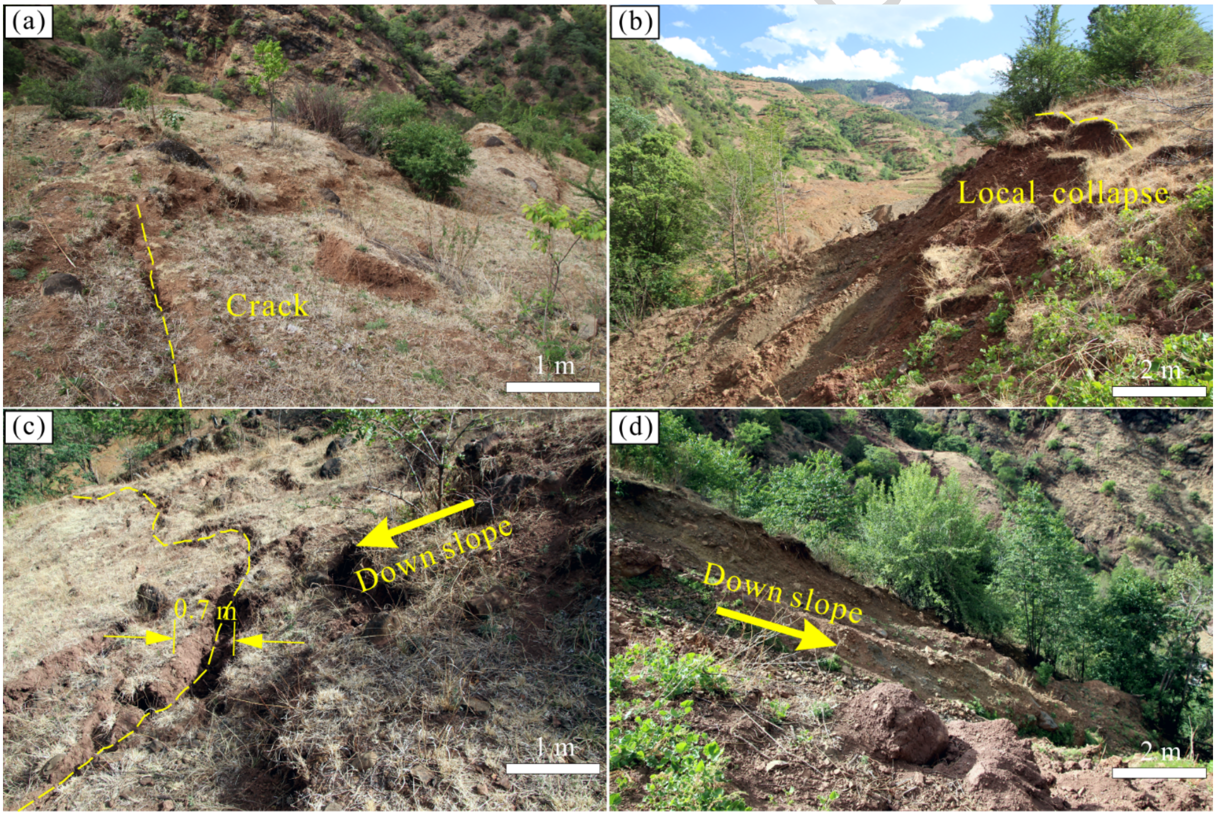

Fig. 8 Deformations observed at the front edge of slope: (a) crack; (b) local collapse occurred on 13 July; (c) Tensile crack and (d) collapse on 18 July

Post-failure runout behaviors

https://doi.org/10.1016/j.compgeo.2023.105455

Fig. 9 depicts the runout process after landslide initiation at eight different time steps, which lasted about 130s from the beginning to the stable accumulation after the 14-day antecedent rainfall. At the initial moment, the landslide began to slide as a result of gravity and seepage force, with the front edge of first failure. At t = 20 s, the sliding mass dammed the Taozi gully and then the soil masses in the middle and rear parts were retrogressed. At t = 60 s, the sliding masses in the middle part of slope moved downslope, resulting in overlap accumulation. At t = 80 s, the sliding masses in the rear part presented compound failure of retrogressive and progressive failure towards the front and middle part of the slope, forming platform-like accumulation landforms. At t = 130 s, the landslide movement terminated. The reactivated landslide reached the furthest elevation of 2338.3 m at the front edge. The final sliding distance was 227.6 m, which was similar to the farthest elevation of 2337.1 m and the maximum sliding distance of 225.4 m obtained in the field evidence. Thus, the simulation results of coupled hydro-mechanical two-phase unsaturated MPM were reasonable.

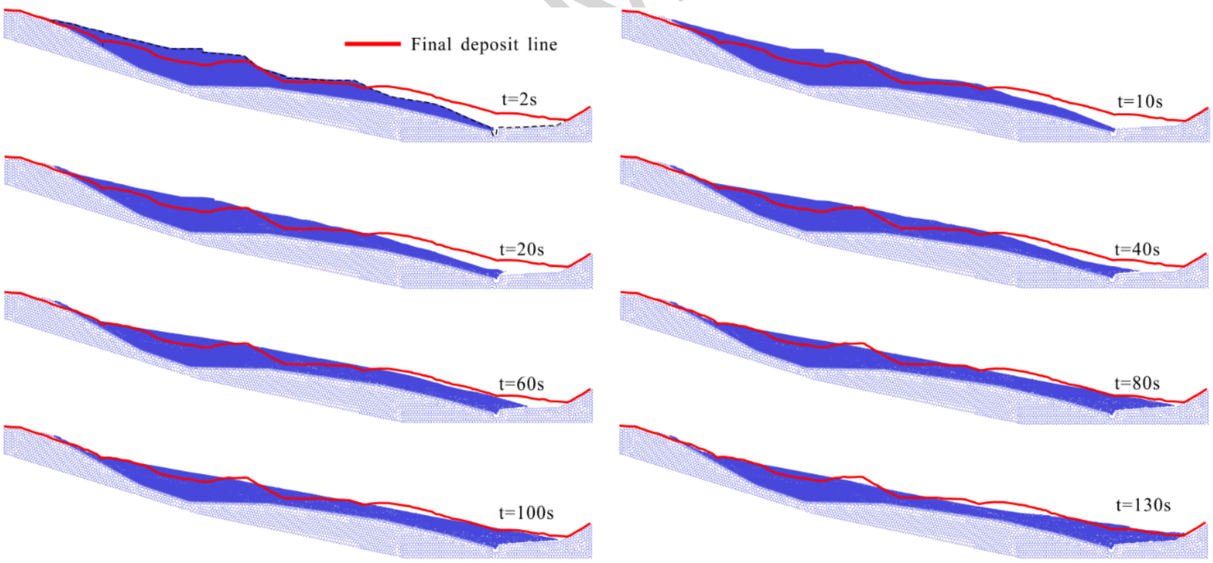

Fig. 9 The runout processes and final landslide deposits compared to field observation

Kinematic behaviors

Fig. 10 illustrates the velocity and displacement distribution at different times of the reactivated landslide. Initially, the soil masses in the front edge began to slide towards the free surface of the right bank of Taozi gully, the front sliding masses entered the gully channel with a velocity of 6 m/s and a displacement of 18 m at t = 5 s. The sliding masses at middle and upper slope began to move, and the velocity reached 5 m/s at the scarp II, and the maximum displacement reached 30 m at the scarp III. The displacement of about 14 m appeared at the backwall at the rear edge. The slope presented uncoordinated movement, and the velocity was concentrated at the micro-geomorphic mutations. Due to friction and collision, the MPs at the bottom of the gully bed had obvious deceleration and accumulation phenomenon, while the MPs at the top still maintained accelerating motion. Meanwhile, the middle and rear velocity concentrated on the MPs in the area with steep slope. At t = 40 s, the velocity of the front sliding masses decreased to 0 when it reached the opposite bank side for a certain distance, with a displacement of 80 m. The middle sliding masses maintained accelerating movement with the velocity of 7.5 m/s and the maximum displacement reached 170m, while the rear sliding mass had the velocity of 5 m/s. After this, the movement of the front sliding masses showed stratified phenomenon. The velocity of the bottom MPs was close to 0 and that of the upper MPs was about 5 m/s, which was subjected to the overloading and shoveling of the following sliding masses. At t = 80 s, the middle sliding masses gradually moved to the leading edge accumulation with a velocity of 12.5 m/s and a maximum displacement of 400 m. The velocity of the rear sliding masses decreased to 0, and the displacement was about 120 m. Influenced by the terrain and the barrier of the anterior accumulation, the landslide was terminated until 130 s, when the overall velocity of the landslide reduced to 0, and the final displacement reached a maximum of 560 m, which belonged to the MPs below the scarp III in the middle of the slope, and matched well with the maximum displacement of 580 m of the reference ground feature mark found in the field investigation (Fig. 11). Thus, it could be inferred that the MPs with the maximum velocity and displacement of landslide were concentrated at scarps of the original slope, instead of the whole movement with the same velocity, and the different movement characteristics of the landslide were significant.

Computers and Geotechnics. Submitted Nov 2022; Published Apr 2023.
https://doi.org/10.1016/j.compgeo.2023.105455

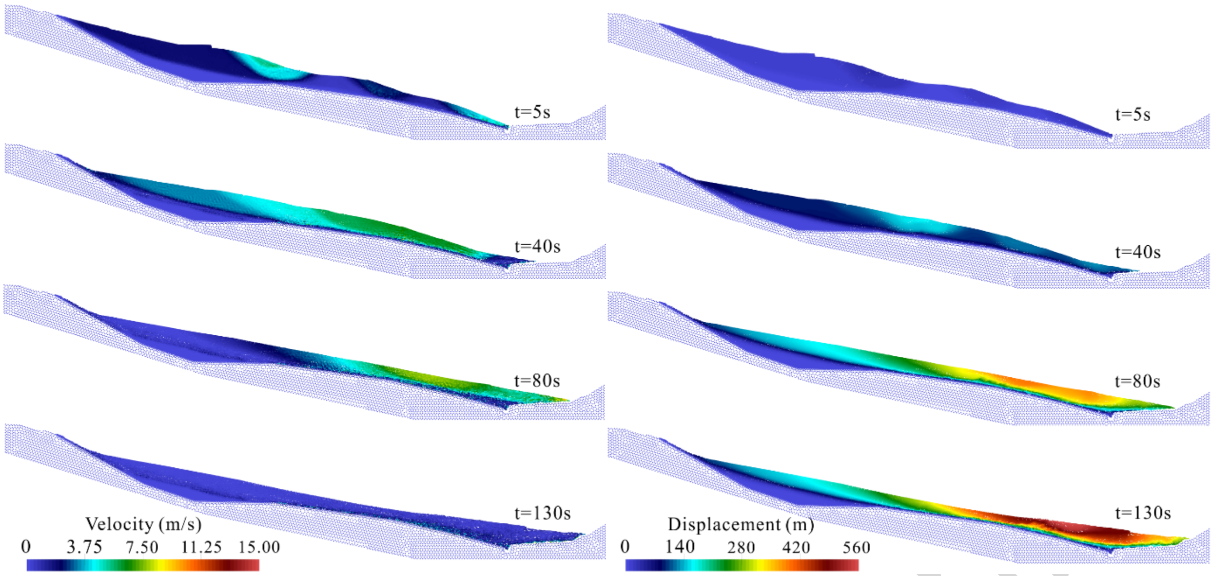

Fig. 10 The kinematic results of MPM: (a) velocity and (b) displacement

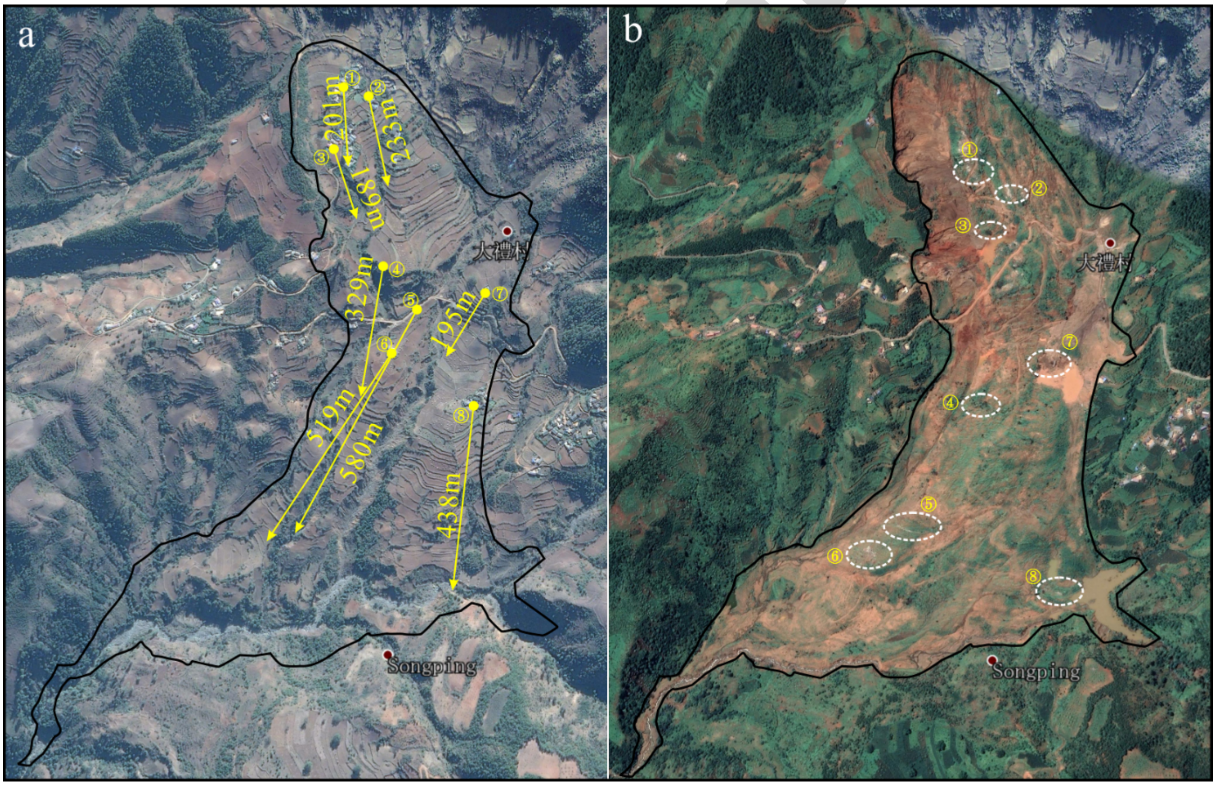

Fig. 11 Motion of ground surface landmarks. (a) November 9, 2015 (b) August 12, 2019 from the Google Earth image

Fig. 12 shows the variation in shear strains at different times. The bottom and interior of the sliding masses experienced intense shear deformation. At t = 2 s, the shear strain concentrated on the front edge of the slope and developed backward along the interface of soil and bedrock. At t = 10 s, the bottom shear zone was obvious at the front edge, the middle edge and the rear edge of the slope. At t = 20 s, the shear zone extended to the surface scarps, with the characteristics of multiple sliding zones. At t = 40 s, the shear strain concentration zone at the bottom is progressively connected, and the multiple shearing was presented in the middle part. At t = 60 s, the shear zone was completely connected. After t = 80 s, the high shear strain area was mainly concentrated in the contact area between the sliding masses and the bedrock, and the sliding mass had internal shear phenomenon in the process of termination.

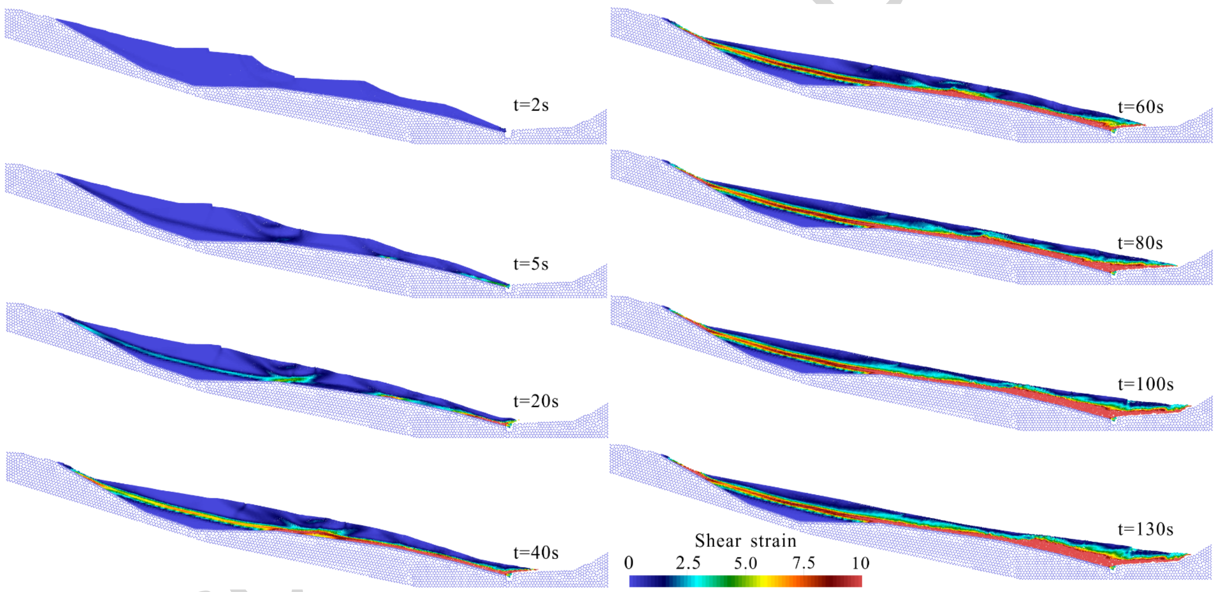

Fig. 12 The strain distribution calculated by MPM

Fig. 13 depicts the distribution of PWP and soil saturation at different times. At beginning, the soils on the front bank slope of Taozi gully reached fully saturated state, and the PWP increased from the initial -150 kPa to 50 kPa. At t = 5 s, the soils slid downward continuously, the irregular slope surface gradually evolved into relatively smooth, and the PWP and saturation at the rear edge increased. Following this, the wetting front of the central sliding masses rose, the PWP increased and the

Computers and Geotechnics. Submitted Nov 2022; Published Apr 2023.
https://doi.org/10.1016/j.compgeo.2023.105455

secondary sliding zone formed. The front sliding masses remained saturated with the movement, but the PWP decreased and dissipated gradually. At t = 40 s, the saturation of surface sliding masses of the rear edge rose rapidly and reached saturated state, and the PWP reached 50 kPa. The rear edge began to slide under the influence of hydraulic pressure, and exerted a pushing effect on the sliding masses below. After t = 80 s, PWP in the front edge accumulation rose again due to the scraping of subsequent sliding masses and continued to move forward under the action of shoveling. The sliding masses at the rear edge basically stopped, and the PWP and saturation remained unchanged, while the PWP inside the sliding masses fluctuated within a certain range, and the soil saturation distribution remained unchanged.

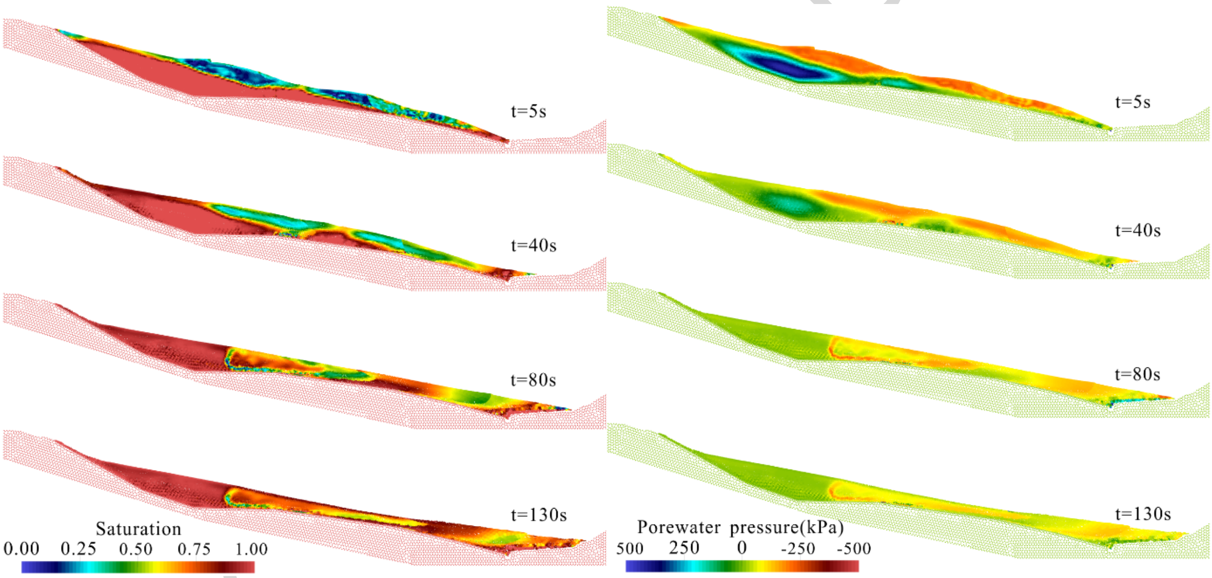

Fig. 13 The seepage results of MPM: (a) saturation and (b) PWP

Figs. 14~17 respectively display the evolution process of velocity, displacement, PWP and saturation of 10 monitoring points, as shown in Fig 5. Point A6 is located near the front edge, the area where the initial deformation occurred. At t = 4 s, A6 reached the maximum velocity of 10 m/s, then began to deposit and the velocity dropped sharply and then, the velocity fluctuated due to the scrapping of the rear sliding masses at about t = 60 s. Point A5, located in the middle section of front edge and

Computers and Geotechnics. Submitted Nov 2022; Published Apr 2023.
https://doi.org/10.1016/j.compgeo.2023.105455

scarp II, began to accelerated by the drag force from the front sliding masses. At t = 26 s the velocity showed a decreasing trend, and then accelerated again at t = 46 s, which corresponds to scraping from the acceleration of the subsequent sliding masses. Fig. showed that two points of A4 and A5 had the same acceleration after t = 46 s, and both reached their maximum velocities at t = 70 s, which were 14 m/s and 10 m/s respectively. Point A3, located at the scarp III, since the start of movement, had entered the accelerated motion with higher acceleration than other points, reaching 9.2 m/s at t= 10s, and then maintaining the velocity until t = 90 s when it began to decelerate. This motion feature resulted in A3 had the largest runout displacement. A2 and A1, located at the rear edge of the slope, had similar movement characteristics. A2 was located at the original topographic platform surface and reached the maximum velocity of 7.5 m/s at 28 s and began to decelerate at 60 s. A1, located on the steep slope of the rear edge, reached the maximum velocity of 5.8 m/s at 35 s, and then began to decelerate, then decreased to 0 at 72 s, indicating that the sliding mass at the rear edge moved for a short time, which was consistent with the motion characteristics of the ground marks in Fig. 11.

Points B1-B4 were located in the bottom part of the sliding mass, having lower velocities that of the surface points. B1 was located near the backwall at the rear edge and had a low velocity, floating within the range of 0~2 m/s, indicating that it only slid slowly along the backwall. B2 and B3 were the deep MPs below the middle of the slope, and both of them presented two-stage accelerated movements, with period of 0~20 s and 30~45 s for B2, and 30~40 s and 50~65 s for B3, wherein the second accelerated movement of B2 was caused by the pushing of the upper sliding mass, and at the same time, it promoted the first accelerated movement of B3 in front. After the front sliding mass moved, the support materials were removed for B3 and it accelerated again and reached a maximum velocity of 7 m/s. B4 is the deep MP of the front edge. The accelerated movement began at t = 0 s, and reached the maximum velocity of 11 m/s at t = 18 s, and then slowed down and moved at a constant velocity. At t = 40 s, the velocity decreased to 2 m/s, which was similar to A6.

Computers and Geotechnics. Submitted Nov 2022; Published Apr 2023.
https://doi.org/10.1016/j.compgeo.2023.105455

The displacement characteristics were highly correlated with the velocity. The maximum displacement of A3 at the middle scarp III was 468.8 m, following by MP A4 at scarp II of 442.4m. The maximum displacement of A5 reached 327.3m. The motion characteristics of A2 and A1 are similar, but the motion duration of A1 was short, the displacement difference was about 120 m compared with that of A2. The velocity of A6 was at a low value after it accumulated in the gully, resulting in a small displacement of 16.3 m.

Among points B1-B4, B4 and A5 were similarly subjected to the action of scraping, with a long duration of movement and a maximum displacement of 88.3 m. The motion characteristics of B2 and B3 were similar, with the maximum displacement of 52.8 m and 41.3 m respectively. B1 had the smallest average velocity, thus the maximum displacement was only 14.8 m, indicating that part of the sliding mass remained in the rear edge area. By monitoring the kinematic characteristics (velocity and displacement), the reactivated landslide presented differential motions in different landforms and depth, further compound retrogressive and progressive failures leaded to scraping effect on sliding mass, which experienced several accelerated motions, reflecting the complexity of the landslide runout. MPM simulation results are highly consistent with the survey evidences.

Computers and Geotechnics. Submitted Nov 2022; Published Apr 2023.
https://doi.org/10.1016/j.compgeo.2023.105455

378 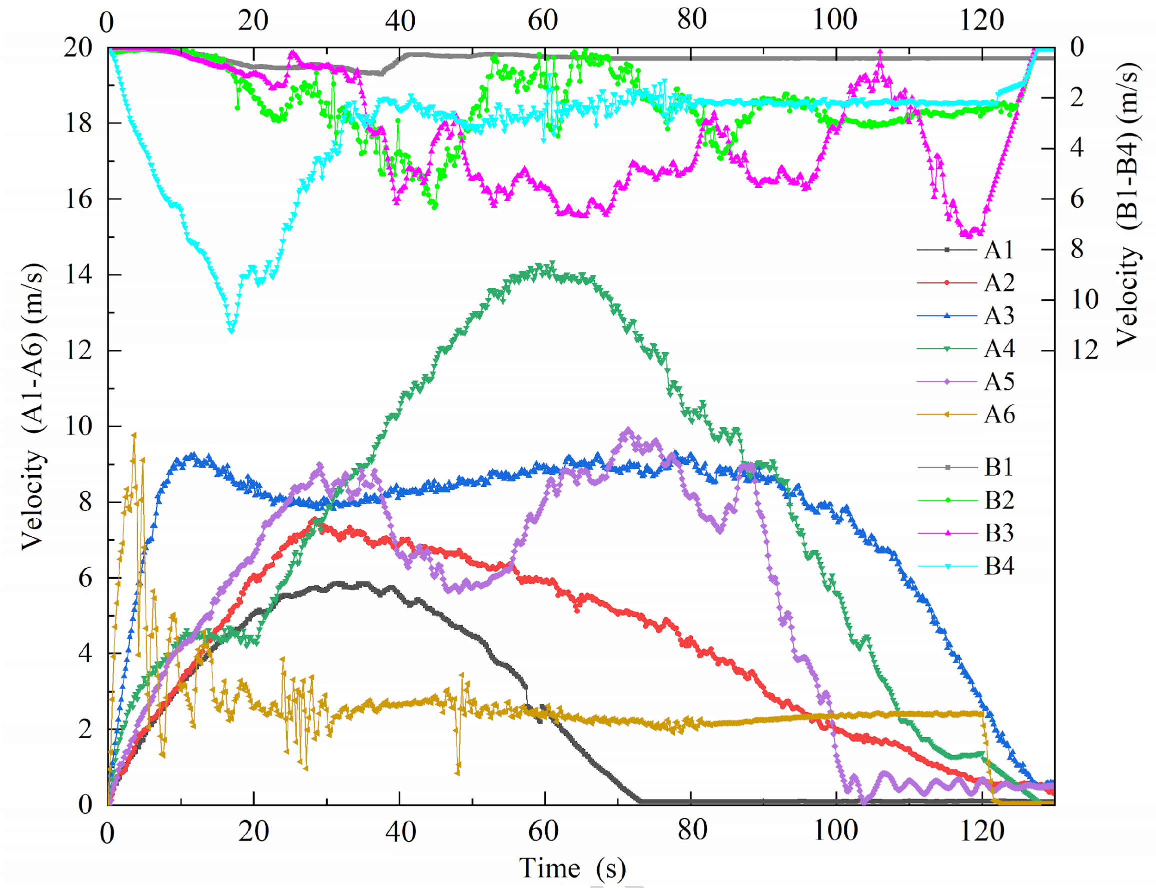

379 Fig. 14 Velocity behavior at different locations

Computers and Geotechnics. Submitted Nov 2022; Published Apr 2023.
https://doi.org/10.1016/j.compgeo.2023.105455

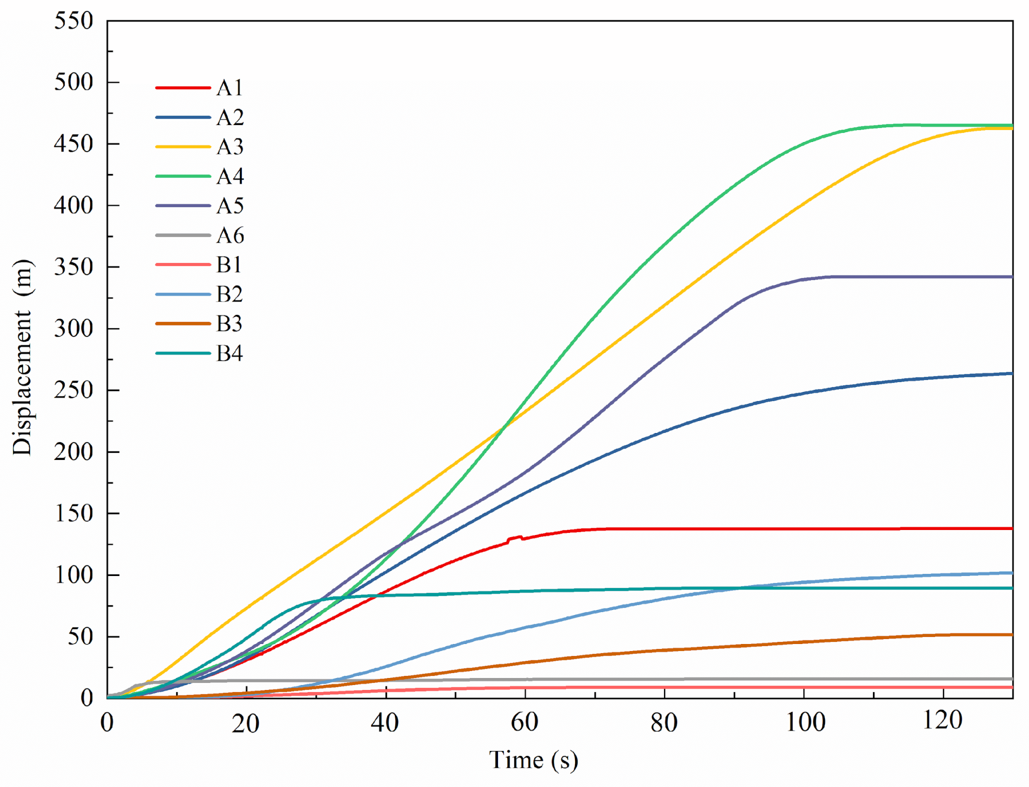

Fig. 15 Displacement behavior at different locations

By comparing the variations of PWP, saturation and kinematic characteristics in the process of landslide movement at the monitoring points, it could be outlined that the PWP generated by rainfall and groundwater seepage was the main driving factor of landslide initiation and movement. After the antecedent rainwater infiltration, the PWP and saturation of surface MPs (A1-A6) continued to rise within 0~2 s, especially A6 on the surface of the front edge of the slope. At t = 2 s, the PWP of A6 reached the maximum value of 50 kPa, followed by local failure in the front and the overall failure stage of the landslide. A6 remained saturated with fluctuated PWP during the landslide. This was due to continuous seepage of groundwater resulted from the subsequent scraping of sliding mass. Points A1-A5 belong to the surface MPs in the middle and rear parts, and their saturation and PWP changed in the same trend, both of which remained basically unchanged in the subsequent landslide movement. B1-B4 were the deep MPs of slope, and B1, B2, B4 were below the initial ground water level, meaning to saturated state. The initial positive PWP presented declining trend during landslide. The PWP and

Computers and Geotechnics. Submitted Nov 2022; Published Apr 2023.
https://doi.org/10.1016/j.compgeo.2023.105455

saturation remained stable when the movement of B1 reached t = 40 s, corresponding to the end of the movement. B2 is located near the secondary slip zone of scarp III (Fig. 44). which was subjected to shearing with the fluctuated PWP. After the secondary shear failure occurred, the PWP and saturation remained unchanged after t = 60 s. B4, located at the front edge, similar to A6, the seepage field changed dramatically, causing larger changes in PWP and saturation than other points. B3 is located above the initial groundwater level, and the change of PWP was similar to that of A2-A5. Due to the inconsistency in the depth, the change of PWP is lagging behind that of the A-series points.

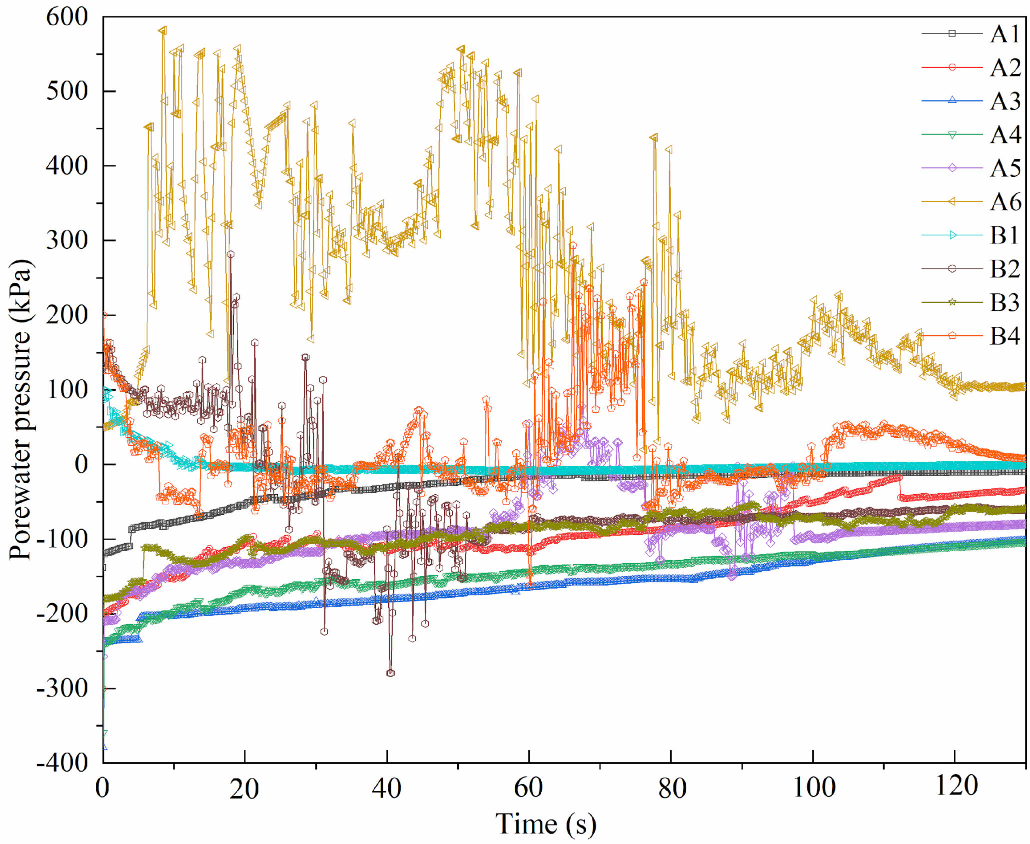

Fig. 16 PWP behavior at different locations

Computers and Geotechnics. Submitted Nov 2022; Published Apr 2023.
https://doi.org/10.1016/j.compgeo.2023.105455

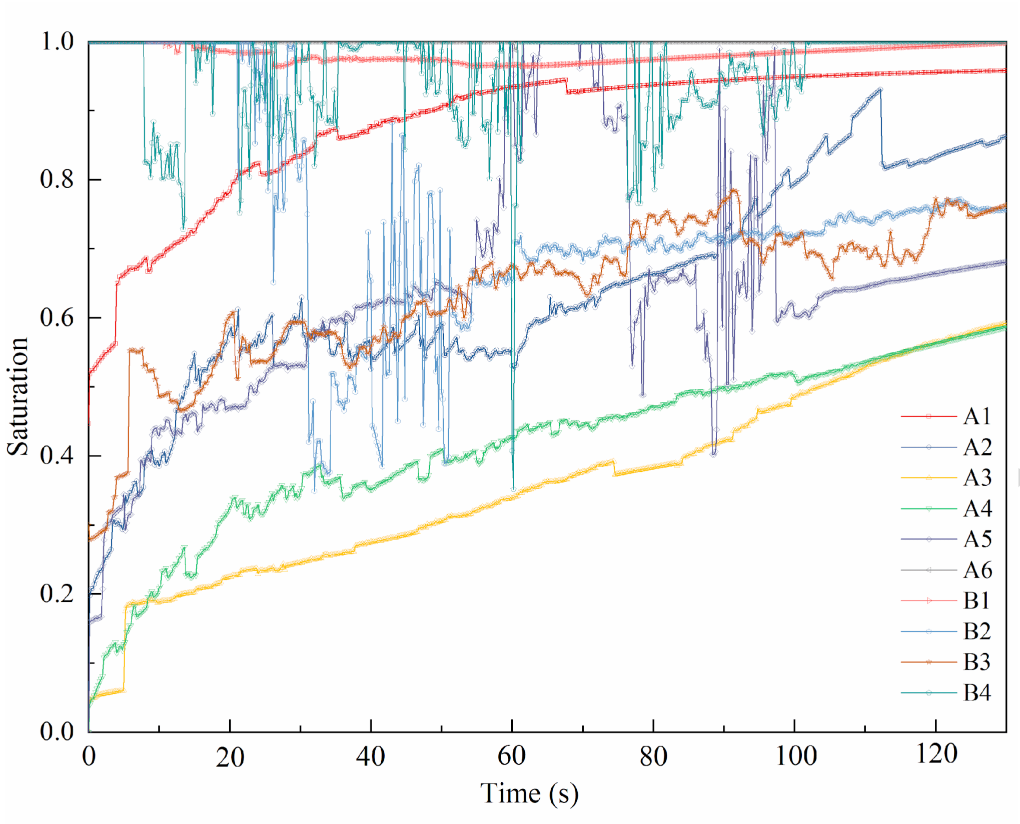

Fig. 17 Saturation behavior at different locations

Discussions

Pre-failure deformation compared with other methods

The results obtained highlight the performance of MPM on outlining the pre-failure deformation analysis. Nevertheless, the classical method in analyzing the pre-failure evolution of the slope is Finite Element Method (FEM). As aforementioned, the seepage from rainfall and groundwater is the prime triggering factor of this reactivated landslide. Here uncoupled seepage FEM with LEM and hydro-mechanical coupled FEM are conducted to compute spatio-temporal distributions of PWP within the slope.

Computers and Geotechnics. Submitted Nov 2022; Published Apr 2023.
https://doi.org/10.1016/j.compgeo.2023.105455

1. Uncoupled seepage FEM with LEM

Firstly, PWP was modelled to calculate the variation induced by antecedent rainfall (14 days). The seepage modelling was conducted through FEM code SEEP/W (Geostudio 2018), with a mesh of 15813 triangular elements with each size of 2 m (Fig. 18). The input parameters are similar to MPM. A flux boundary condition equal to the daily rainfall intensities (Fig. 4) was applied at the ground surface. Then the LEM, Morgenstern-Price method based on Slope/w (Geostudio 2018), was used to compute the stability factor of the slope, and the extended Mohr-Coulomb failure criterion for unsaturated soils was considered.

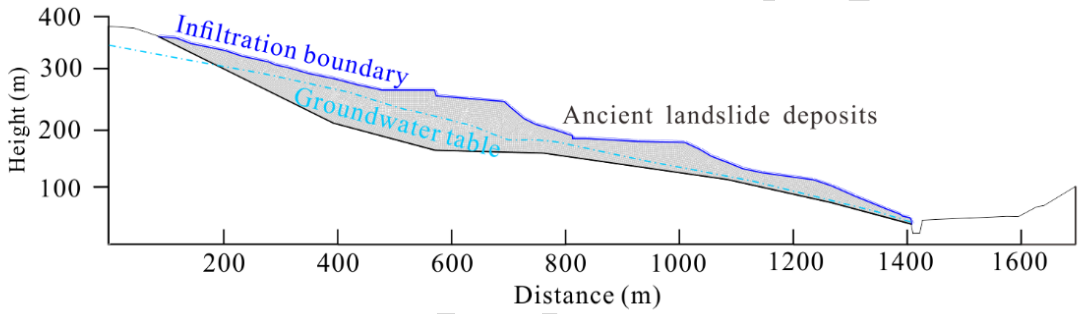

Fig. 18 Computational uncoupled seepage FEM mesh used for the seepage analysis

PWP results were used as input data for slope stability analysis in LEM analyses to evaluate the spatio-temporal evolution of stability factors along shallow or deep sliding surfaces during rainfall infiltration. 382 curved and foldline sliding surfaces at the front edge of the slope were specified through the central grid and radius range.

Fig. 19 depicts the spatial distribution of *Fs* computed for four reference times. The slope is simulated as initially stable (Fig. 19a) and remains stable during the first five days of rainfall, with the *Fs* greater than 1.1 at any front sliding surface, while the groundwater level gradually is rising (Fig. 19b). The Fs drops to lower than 1.1 along a sliding surface after seven days rainfall (Fig. 19c). The deep sliding surface reaches an unstable state after 14 days of rain (Fig. 19d). For the sliding surface

Computers and Geotechnics. Submitted Nov 2022; Published Apr 2023.
https://doi.org/10.1016/j.compgeo.2023.105455

with different depths at the front of slope, the *Fs* gradually decreases with the infiltration of rainwater, and gradually extends from the shallow sliding surface to the deep sliding surface. This change of slope stability is consistent with the retrogressive failure mechanism.

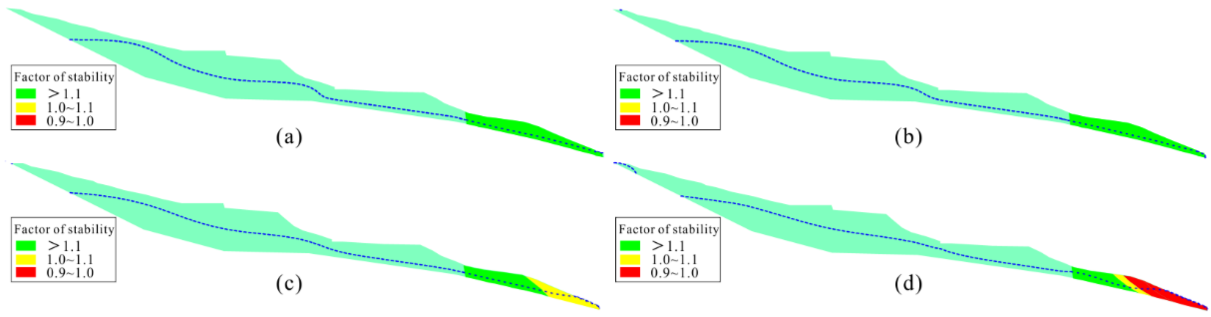

Fig. 19 Factor of stability spatial distribution for (a) t = 0 day; (b) t = 5 days; (c) t = 7 days; (d) t = 14 days

Fig. 20 illustrates the changes in *Fs* of sliding surfaces of different depths (shallow and deep), indicating that the stability of shallow sliding mass at the front edge reduces over time under the influence of rainfall and groundwater seepage, which drops to lower than 1.0 on July 13, when the daily rainfall reached 69.4 mm, the *Fs* decreased to 0.993, which is in an unstable state (Fig. 20a). The result is consistent with the collapse of the front slope before the large-scale reactivated landslide occurrence. The deep sliding surface presents a slower reduction of *Fs* over the time (Fig. 20b). By analyzing the calculated results of the time-trend of *Fs*, it can be deduced that the stability of the front part of slope presents different decreasing trends with the rainfall duration, which is closely related to daily rainfall intensities.

LEM coupled seepage analysis achieves a conclusion consistent with field investigation in the analysis of groundwater level change and slope stability. For shallow sliding surface and deep sliding surface, the stability coefficient decreases to below 1.0 approximately when the local collapse phenomenon occurs at the front edge of the slope. However, more sophisticated analysis is required to

https://doi.org/10.1016/j.compgeo.2023.105455

better understand the compound mechanism of from the onset of the front edge failure to the subsequent overall sliding.

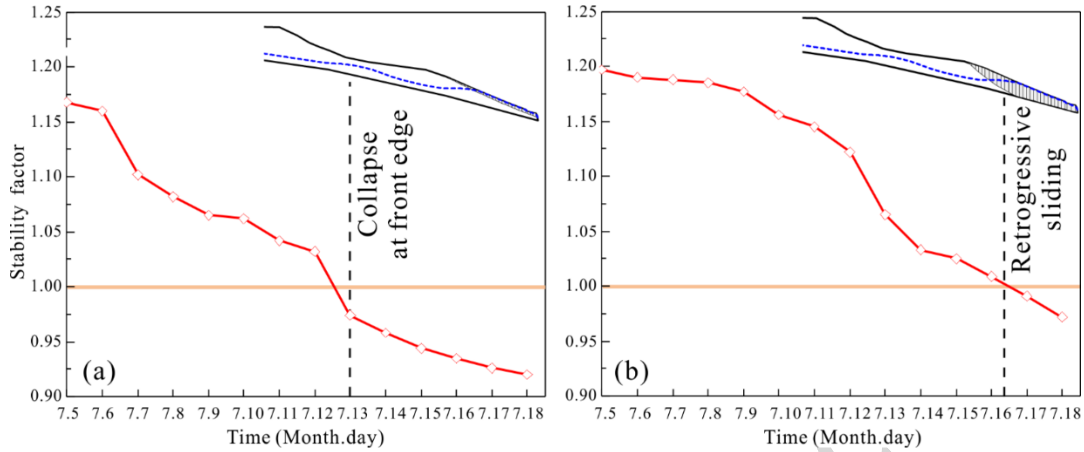

Fig. 20 Factor of stability changing in time along (a) shallow and (b) deep sliding surface

2. Hydro-mechanical coupled FEM

Hydro-mechanical coupled FEM was conducted using software RS2 Rocsciences (Rocscience Inc 2018) to explore the small-deformation and seepage prior to the slope failure. The model was made of 19702 6-noded triangular elements for sliding mass with a size of 2 m and local refined in the front edge, and 3388 elements for bedrock (Fig. 21). The bottom of the model was fully fixed in the X and Y directions, and the left and right edges were fixed in the X directions. The input parameters are the same as MPM. After calculating the initial equilibrium geo-stress, the solid-liquid coupled deformation analysis was carried out to simulate the rise of PWP and groundwater level caused by rainfall infiltration. The complete implicit integration scheme is used in the plane-strain condition, which allows large time step and fast calculation. Six monitoring points were set at the front edge and the middle of the slope (Fig. 21) to calculate the time-trend of displacement, so as to compare the numerical analysis results with the in-situ failure phenomena before the landslide.

Computers and Geotechnics. Submitted Nov 2022; Published Apr 2023.
https://doi.org/10.1016/j.compgeo.2023.105455

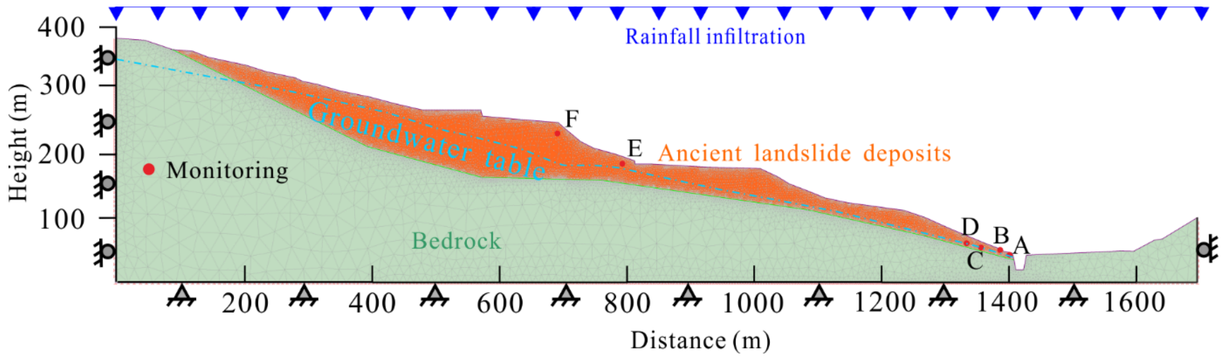

Fig. 21 Computational hydro-mechanical coupled FEM mesh

Fig. 22 shows the FEM-derived displacements of monitoring points over the time. The deformation of the front edge is much larger than that of the middle part, and the variation trend of the front edge displacement is consistent with the variation of daily rainfall intensity. The cumulative rainfall in the first 6 days was 112.5 mm, and the maximum daily rainfall occurred on July 5, which was 58.1mm. The displacement increased slowly at this stage, and the maximum cumulative displacement was 0.43m in the front edge. From the seventh day to the ninth day, the cumulative rainfall reached 148mm in three days, and the maximum rainfall intensity occurred on July 13, when the maximum displacement of the front edge reached 0.90 m, and then local collapse occurred. From the deformation of monitoring points at different depths, the deformation of points on the slope surface (A, B) was larger than that of points at deeper depths (C, D), which is consistent with the field investigation phenomenon of retrogressive sliding. After July 13, the middle part of the slope began to deform rapidly. Fig. 23 presents the maximum shear strain distribution of the slope after the rainfall infiltration. The shear strain at the front edge was concentrated through the area, and a potential sliding zone at the central scarp was formed.

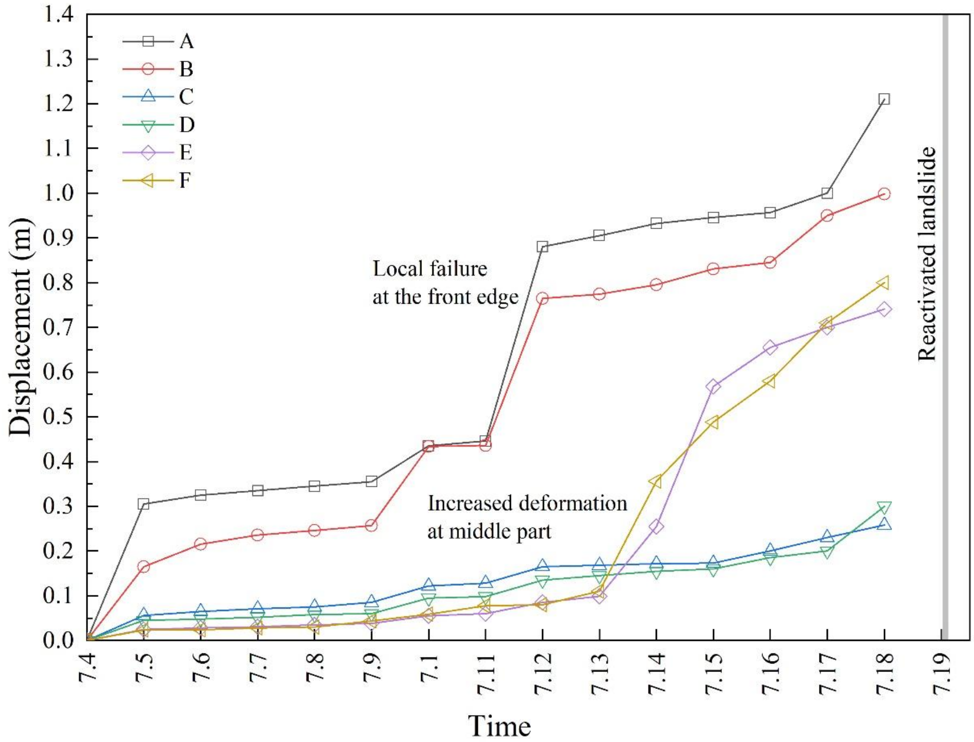

Fig. 22 Displacements of monitoring points over time obtained by FEM

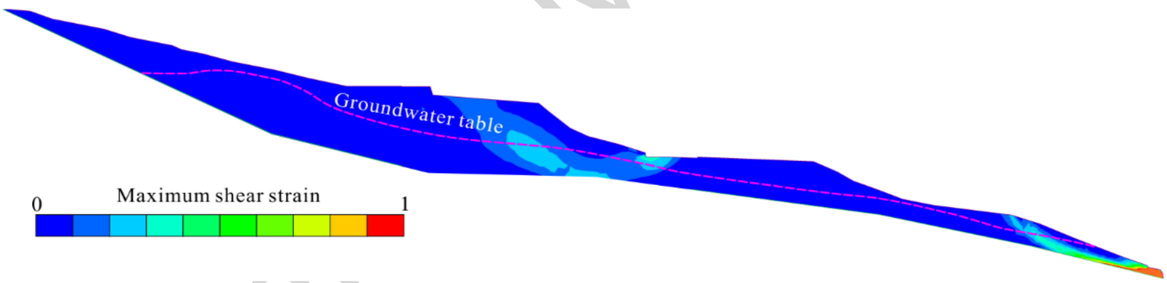

Fig. 23 Maximum shear strain distribution after 14 days of rain

Fig. 24 demonstrate the PWP spatio-temporal distribution obtained by three different methods. A good agreement among three results is observed, including the unsaturated zone and groundwater table. The PWP time-trend of two monitoring points located in the front (P1) and middle (P2) parts provide more insights (Fig. 25). At P1 the computed PWP increased slowly at the first 5 days of rain, indicating the stable state of the front slope. Then the PWP suddenly increased with a high increasing rate until July 14, showing the occurrence of the local collapse at July 13, the time reported by eyewitnesses. At

Computers and Geotechnics. Submitted Nov 2022; Published Apr 2023.
https://doi.org/10.1016/j.compgeo.2023.105455

P2, the PWP grew suddenly after the first day of rain and then increased slightly before the large-scale retrogressive failure occurred.

As a major limitation, the post-failure is not simulated by FEM due to the computation terminates once the large deformation occurs. Thus, the results achieved by MPM outline the good performance in simulating the entire process (pre-failure and post-failure) of such compound landslides.

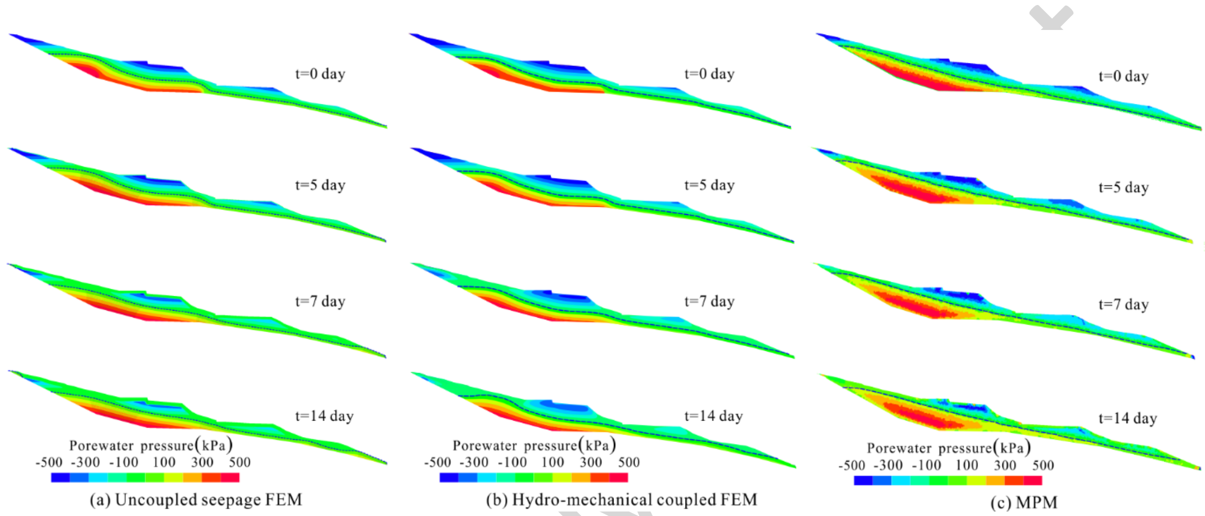

Fig. 24 PWP distribution: (a) Uncoupled seepage FEM; (b) Hydro-mechanical coupled FEM; (c) MPM

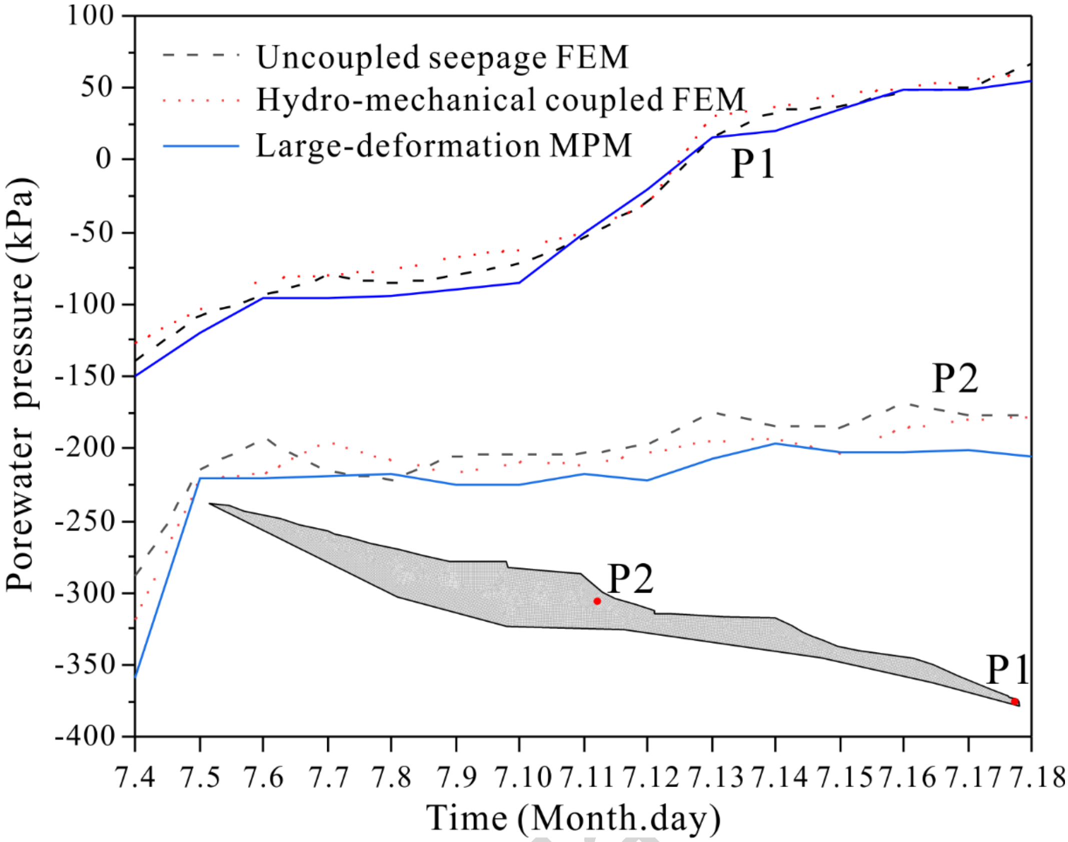

Fig. 25 Comparison among uncoupled seepage FEM, hydro-mechanical coupled FEM and MPM analysis in terms of PWP over time at two monitoring points

Post-failure runout affected by analysis type

In order to further explore the influence of pre-existing groundwater and antecedent rainfall on the landslide runout behaviors, three different conditions were considered to simulate the runout distance of landslide. Conditions include unsaturated soil with only groundwater, unsaturated soil with only rainfall, and full-saturated soil without groundwater and rainfall. Other settings of the models are consistent with those described in Method section.

Fig. 26 displays the comparison of the final landslide deposits geometry through four analysis types. The results show that in the unsaturated two-phase simulation considered both groundwater and rainfall, the maximum displacement of MPs was 560 m, and the largest runout distance was 227.6 m, while the largest runout distance measured in the field was 225.4 m. When only the pre-existing groundwater was considered, the maximum displacement of the MPs was 322 m and the largest runout distance was 184.5 m. Considering only antecedent rainfall infiltration, the maximum displacement was 340 m and the distance was 157.6 m. When full-saturated simulation is adopted, the maximum displacement of MPs was 820 m, and the largest runout distance is 290 m, which was much larger than the actual displacement and runout distance. In addition, the simulation results of unsaturated two-phase are closer to the actual accumulation morphology. These results show that the unsaturated two-phase simulation has a good performance on the simulation of landslide runout by the influence of hydraulic-related seepage. The pre-existing groundwater and antecedent rainfall are the main inducing factors to the landslide runout.

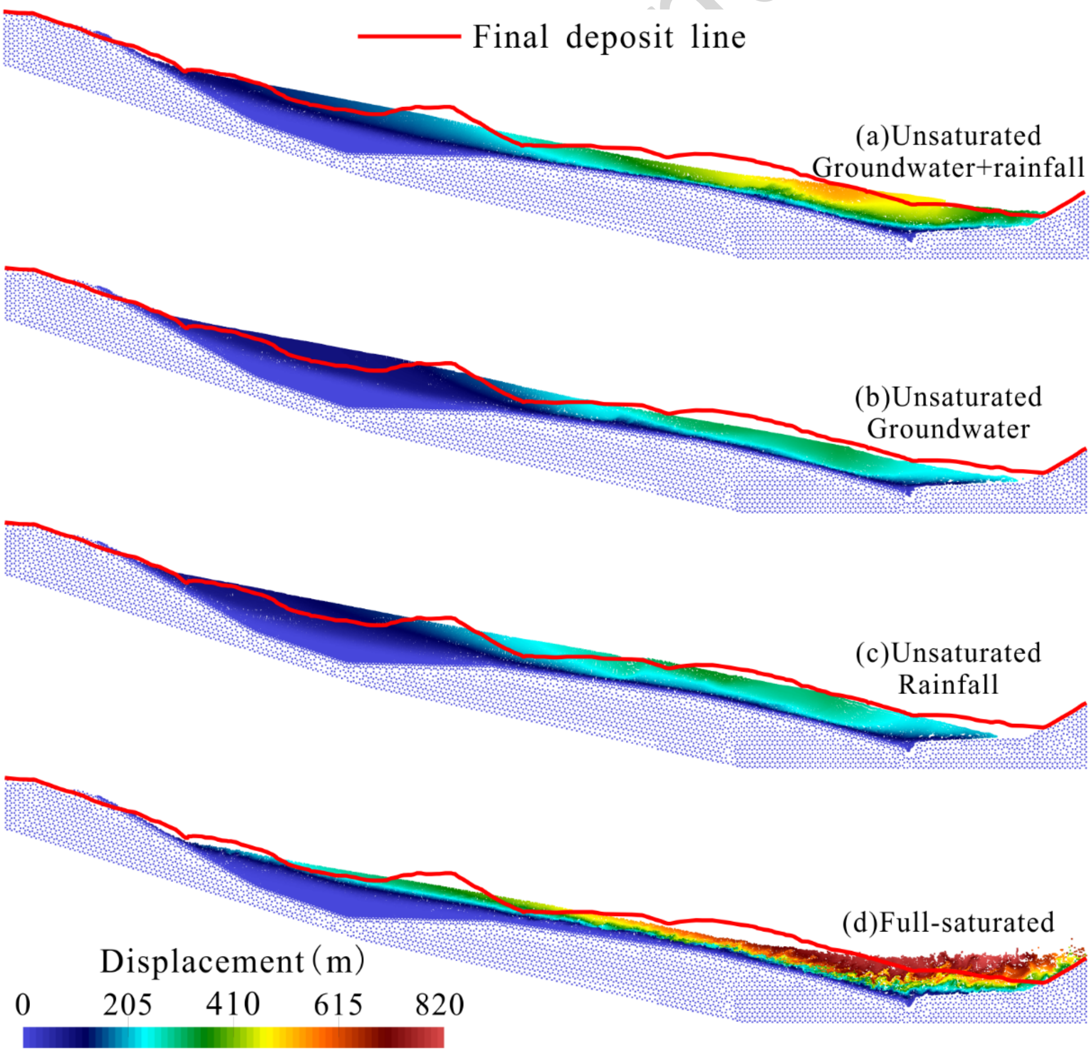

Fig. 26 Comparison of the final landslide deposits geometry computed by different types of analyses: unsaturated condition: (a) considering groundwater and rainfall; (b) considering groundwater; (c) considering rainfall. (d) full-saturated condition

Limitations

Albeit the results derived from this study have largely coincided with the field observations, some deficiencies still exist. Firstly, the presented study focuses on examining the pre- and post-failure behaviors in terms of kinematic, seepage and strain of a landslide with a 2D cross section, which is a preliminary research serving as the basis for exploring more realistic landslides (Lei et al. 2020). Ideal slopes were adopted with neglection of terrain irregularity and variations in moving width direction were not considered to facilitate efficient computation. Nonetheless, 2D modeling disenables us to capture crucial such behaviors in all directions of interest (Li et al. 2020). A sophisticated 3D modeling can simulate, over complex topography, different regimes of landslides with unprecedented details (Li et al. 2021; Lei et al. 2022). Future studies will consider real 3D topography and recover the lateral boundary conditions of landslides. Secondly, in the present simulation, soils were taken as homogeneous bodies, and the soil anisotropic properties such as cohesion and friction angle were not considered. The deterministic analysis of landslide runout with the assumption that the shear strength parameters are isotropic have been proved in previous studies (Yerro et al. 2019; Cuomo et al. 2021b; Nguyen et al. 2022; Kohler and Puzrin 2022; Ying et al. 2021). Albeit the isotropic analysis is used for simulation of a specific slope, and reveals the runout behavior of landslide, it is a useful method and can be extended to consider inherent spatial variability of soil properties, such as cohesion, friction angle (Liu et al. 2019; Ma et al. 2022a, b). Previous studies indicated that ignoring the spatial variability of soil shear strength might result in overestimation or underestimation in landslide runout analysis. In consequence, the probabilistic post-failure analysis of landslides should be considered in future works. Lastly, we used a constant value of cohesion during runout simulation, which although showed a good agreement with field observations, the actual variation of soil strength may still differ from a constant and high value once it failed and began to move. Hence, a potential strength reduction in the soil mass during landslide movement might lead to larger landslide deformations and more precisely accumulational geometry. Thus, more advanced models, such as MC strain-softening model, Drucker-Prager model, which will be carefully considered in the future works.

Conclusions

This paper explores the pre- and post-failure behaviors of a compound reactivated landslide induced by antecedent rainfall and groundwater seepage by using a single-point two-phase MPM. The numerical results are examined to reveal the pre-failure deformation mechanism and post-failure runout of landslide. Moreover, the pre-failure results are compared with the classical FEM, and the effect of soil conditions and factors during landslide on final landslide deposits are discussed. The main conclusions are as follows:

1. The pre-failure behavior of the landslide occurs retrogressively from the front to rear slope. The sliding soils are subjected to the rapid infiltration in the early stage, with the decreasing of negative PWP of surface soils. The front sliding soils reach saturated state firstly, with larger shear strain and displacement than middle and rear parts. During the rainfall, deformations can be more clearly observed at the middle and rear parts of slope, specifically at the scarps.

2. Uncoupled seepage FEM and hydro-mechanical coupled FEM provide similar quantitative indications towards the pre-failure behaviors influenced by the pre-existing groundwater and antecedent rainfall. These standard tools validate the performance of MPM on simulating landslide failure mechanisms.

3. The duration of landslide movement is about 130 s, with a maximum velocity of 15 m/s, and the maximum displacement of 560 m. The kinematic characteristics (velocity and displacement) of the

Computers and Geotechnics. Submitted Nov 2022; Published Apr 2023.
https://doi.org/10.1016/j.compgeo.2023.105455

monitoring points show that the reactivated landslide presents different sliding features with different microtopography and depths. The simulation results of unsaturated two-phase MPM match well with the measured accumulation morphology, which indicates that the simulation of unsaturated two-phase MPM has a good performance on the simulation of landslide runout under the role of hydraulic seepage. The pre-existing groundwater and antecedent rainfall are the main contributing factors to the landslide runout.

CRediT authorship contribution statement

Kun He: Methodology, Software, Data processing, Writing-original draft**. Chuangjie Xi:** Methodology, Validation, Writing-review & editing. **Bo Liu:** Investigation, Methodology, Writing-review & editing. **Xiewen Hu:** Supervision, Funding, Conceptualization, Writing-review & editing. **Gang Luo:** Funding, Writing-review & editing. **Guotao Ma:** Writing-review & editing. **Ruichen Zhou:** Writing-review & editing.

Declaration of Competing Interest

The authors declare that they have no known competing financial interests or personal relationships that could have appeared to influence the work reported in this paper.

Data Availability Statement

All data, models, and code generated or used during the study appear in the submitted article.

Acknowledgments

The authors gratefully acknowledge support from the National Natural Science Foundation of China (41731285), and the China Scholarship Council (NO. 202107000060).

References

Abe, K., Soga, K., Bandara, S. (2014). Material point method for coupled hydromechanical problems. Journal of Geotechnical and Geoenvironmental Engineering, 140(3), 04013033.

Anura3D MPM Research Community (2022). Anura3D Version 2022 Source Code, www.anura3d.com.

Bandara, S., Ferrari, A., Laloui, L. (2016). Modelling landslides in unsaturated slopes subjected to rainfall infiltration using material point method. International Journal for Numerical and Analytical Methods in Geomechanics, 40(9), 1358-1380.

Bandara, S., Soga, K. (2015). Coupling of soil deformation and pore fluid flow using material point method. Computers and geotechnics, 63, 199-214.

Bertolini, G., Pizziolo, M. (2008). Risk assessment strategies for the reactivation of earth flows in the Northern Apennines (Italy). Engineering Geology, 102(3-4), 178-192.

Biot, M. A. (1941). General theory of three - dimensional consolidation. Journal of applied physics, 12(2), 155-164.

Bishop, A. W. (1955). The use of the slip circle in the stability analysis of slopes. Geotechnique, 5(1), 7-17.

Borja, R. I., White, J. A., Liu, X., Wu, W. (2012). Factor of safety in a partially saturated slope inferred from hydro - mechanical continuum modeling. International Journal for Numerical and Analytical Methods in Geomechanics, 36(2), 236-248.

Ceccato, F., Girardi, V., Yerro, A., Simonini, P. (2019). Evaluation of dynamic explicit MPM formulations for unsaturated soils.

Ceccato, F., Yerro, A., Girardi, V., Simonini, P. (2021). Two-phase dynamic MPM formulation for unsaturated soil. Computers and Geotechnics, 129, 103876.

Chen, C. M., Shyu, J. B. H., Tsui, H. K., Hsieh, Y. C. (2022). Preservation and transportation of large landslide deposits under decadal and millennial timescales in the Taiwan orogenic belt. Geomorphology, 415, 108402.

Chen, X., Zhang, L., Zhang, L., Zhou, Y., Ye, G., Guo, N. (2021). Modelling rainfall-induced landslides from initiation of instability to post-failure. Computers and Geotechnics, 129, 103877.

Cui, Y., Deng, J., Hu, W., Xu, C., Ge, H., Wei, J., Zheng, J. (2021). 36Cl exposure dating of the Mahu Giant landslide (Sichuan Province, China). Engineering Geology, 285, 106039.

Cuomo, S., Perna, A. D., Martinelli, M. (2021a). Material point method (MPM) hydro-mechanical modelling of flows impacting rigid walls. Canadian Geotechnical Journal, 58(11), 1730-1743.

Cuomo, S., Perna, A. D., Martinelli, M. (2021b). Modelling the spatio-temporal evolution of a rainfall-induced retrogressive landslide in an unsaturated slope. Engineering Geology, 294, 106371.

de Vaucorbeil, A., Nguyen, V. P., Sinaie, S., Wu, J. Y. (2020). Material point method after 25 years: Theory, implementation, and applications. Advances in applied mechanics, 53, 185-398.

Darrow, M. M., Nelson, V. A., Grilliot, M., Wartman, J., Jacobs, A., Baichtal, J. F., Buxton, C. (2022). Geomorphology and initiation mechanisms of the 2020 Haines, Alaska landslide. Landslides, 1-12.

Feng, K., Huang, D., Wang, G. (2021). Two-layer material point method for modeling soil–water interaction in unsaturated soils and rainfall-induced slope failure. Acta Geotechnica, 16(8), 2529-

2551.

François, B., Tacher, L., Bonnard, C., Laloui, L., Triguero, V. (2007). Numerical modelling of the hydrogeological and geomechanical behaviour of a large slope movement: the Triesenberg landslide (Liechtenstein). Canadian Geotechnical Journal, 44(7), 840-857.

Gariano, S. L., Guzzetti, F. (2016). Landslides in a changing climate. Earth-Science Reviews, 162, 227-252.

Geostudio Manual. (2018). Geo-slope international Ltd. Calgary, Alberta, Canada T2P 2Y5.

GiD. (2018). The personal pre and post processor. Barecelona, Spain: CIMNE, www.gidhome.com.

Haque, U., Da Silva, P. F., Devoli, G., Pilz, J., Zhao, B., Khaloua, A., ... Glass, G. E. (2019). The human cost of global warming: Deadly landslides and their triggers (1995–2014). Science of the Total Environment, 682, 673-684.

He, K., Ma, G., Hu, X., Liu, B. (2021). Failure mechanism and stability analysis of a reactivated landslide occurrence in Yanyuan City, China. Landslides, 18(3), 1097-1114.

He, K., Ma, G., Hu, X., Liu, B., Han, M. (2022). The July 2, 2017, Lantian landslide in Leibo, China: mechanisms and mitigation measures. Geomech Eng, 28(3), 283-298.

He, X., Liang, D., Bolton, M. D. (2018). Run-out of cut-slope landslides: mesh-free simulations. Géotechnique, 68(1), 50-63.

Jamalinia, E., Vardon, P. J., Steele-Dunne, S. C. (2020). The impact of evaporation induced cracks and precipitation on temporal slope stability. Computers and Geotechnics, 122, 103506.

Janbu, N. (1954). Application of composite slip surface for stability analysis. In Proceedings of

European Conference on Stability of Earth Slopes, Sweden, 3, 43-49.

Jassim, I., Stolle, D., Vermeer, P. (2013). Two-phase dynamic analysis by material point method. International Journal for numerical and analytical methods in geomechanics, 37(15), 2502-2522.

Jiang, C., Schroeder, C., Teran, J., Stomakhin, A., Selle, A. (2016). The material point method for simulating continuum materials. In ACM SIGGRAPH 2016 Courses, 1-52.

Jiang, N., Li, H. B., Hu, Y. X., Zhang, J. Y., Dai, W., Li, C. J., Zhou, J. W. (2022). Dynamic evolution mechanism and subsequent reactivated ancient landslide analyses of the “6.17” Danba sequential disasters. Bulletin of Engineering Geology and the Environment, 81(4), 1-16.

Kafaji, I. K. A. (2013). Formulation of a dynamic material point method (MPM) for geomechanical problems. M. Sc. thesis, Department of Geotechnics, Universität Stuttgart, Stuttgatt, Germany.

Kim, J., Hwang, W., Kim, Y. (2018). Effects of hysteresis on hydro-mechanical behavior of unsaturated soil. Engineering Geology, 245, 1-9.

Kohler, M., Puzrin, A. M. (2022). Mechanism of Co-Seismic Deformation of the Slow-Moving La Sorbella Landslide in Italy Revealed by MPM Analysis. Journal of Geophysical Research: Earth Surface, 127(7), e2022JF006618.

Lei, X., He, S., Chen, X., Wong, H., Wu, L., Liu, E. (2020). A generalized interpolation material point method for modelling coupled seepage-erosion-deformation process within unsaturated soils. Advances in Water Resources, 141, 103578.

Lei, X., Chen, X., Yang, Z., He, S., Zhu, L., Liang, H. (2022). A simple and robust MPM framework for modelling granular flows over complex terrains. Computers and Geotechnics, 149, 104867.

Li, X., Sovilla, B., Jiang, C., Gaume, J. (2020). The mechanical origin of snow avalanche dynamics

Computers and Geotechnics. Submitted Nov 2022; Published Apr 2023.
https://doi.org/10.1016/j.compgeo.2023.105455

and flow regime transitions. The Cryosphere, 14(10), 3381-3398.

Li, X., Sovilla, B., Jiang, C., Gaume, J. (2021). Three-dimensional and real-scale modeling of flow regimes in dense snow avalanches. Landslides, 18(10), 3393-3406.

Liang, W., Zhao, J. (2019). Multiscale modeling of large deformation in geomechanics. International Journal for Numerical and Analytical Methods in Geomechanics, 43(5), 1080-1114.

Liu, X., Wang, Y., Li, D. Q. (2019). Investigation of slope failure mode evolution during large deformation in spatially variable soils by random limit equilibrium and material point methods. Computers and Geotechnics, 111, 301-312.

Liu, X., Wang, Y. (2021). Probabilistic simulation of entire process of rainfall-induced landslides using random finite element and material point methods with hydro-mechanical coupling. Computers and Geotechnics, 132, 103989.

Luo, G., Hu, X., Bowman, E. T., Liang, J. (2017). Stability evaluation and prediction of the Dongla reactivated ancient landslide as well as emergency mitigation for the Dongla Bridge. Landslides, 14(4), 1403-1418.

Ma, G., Rezania, M., Nezhad, M. M. (2022a). Stochastic assessment of landslide influence zone by material point method and generalized geotechnical random field theory. International Journal of Geomechanics, 22(4), 04022002.

Ma, G., Rezania, M., Mousavi Nezhad, M., Hu, X. (2022b). Uncertainty quantification of landslide runout motion considering soil interdependent anisotropy and fabric orientation. Landslides, 19(5), 1231-1247.

Ma, S., Qiu, H., Hu, S., Yang, D., Liu, Z. (2021). Characteristics and geomorphology change detection analysis of the Jiangdingya landslide on July 12, 2018, China. Landslides, 18(1), 383-396.

Martinelli, M., Lee, W. L., Shieh, C. L., Cuomo, S. (2020). Rainfall boundary condition in a multiphase Material Point Method. Fifth World Landslide Forum, November 2-6, 2020, Kyoto, Japan.

Masoudian, M. S., Afrapoli, M. A. H., Tasalloti, A., Marshall, A. M. (2019). A general framework for coupled hydro-mechanical modelling of rainfall-induced instability in unsaturated slopes with multivariate random fields. Computers and Geotechnics, 115, 103162.

Morgenstern, N. U., Price, V. E. (1965). The analysis of the stability of general slip surfaces. Geotechnique, 15(1), 79-93.

Nguyen, T. S., Yang, K. H., Wu, Y. K., Teng, F., Chao, W. A., Lee, W. L. (2022). Post-failure process and kinematic behavior of two landslides: Case study and material point analyses. Computers and Geotechnics, 148, 104797.

Notti, D., Wrzesniak, A., Dematteis, N., Lollino, P., Fazio, N. L., Zucca, F., Giordan, D. (2021). A multidisciplinary investigation of deep-seated landslide reactivation triggered by an extreme rainfall event: a case study of the Monesi di Mendatica landslide, Ligurian Alps. Landslides, 18(7), 2341-2365.

Peranić, J., Mihalić Arbanas, S., Arbanas, Ž. (2021). Importance of the unsaturated zone in landslide reactivation on flysch slopes: observations from Valići Landslide, Croatia. Landslides, 18(12), 3737-3751.

Peruccacci, S., Brunetti, M. T., Gariano, S. L., Melillo, M., Rossi, M., Guzzetti, F. (2017). Rainfall thresholds for possible landslide occurrence in Italy. Geomorphology, 290, 39-57.

Rocscience Inc. (2018) Rocscience Inc RS2-2D finite element analysis of geotechnical structures Canada, Toronto, Version 9.0.

Scaringi, G., Loche, M. (2022). A thermo-hydro-mechanical approach to soil slope stability under climate change. Geomorphology, 401, 108108.

Soga, K., Alonso, E., Yerro, A., Kumar, K., Bandara, S. (2016). Trends in large-deformation analysis of landslide mass movements with particular emphasis on the material point method. Géotechnique, 66(3), 248-273.

Su, Z., Wang, G., Wang, Y., Luo, X., Zhang, H. (2022). Numerical simulation of dynamic catastrophe of slope instability in three Gorges reservoir area based on FEM and SPH method. Natural Hazards, 111(1), 709-724.

Sulsky, D., Chen, Z., Schreyer, H. L. (1994). A particle method for history-dependent materials. Computer methods in applied mechanics and engineering, 118(1-2), 179-196.

Tang, H., Wasowski, J., Juang, C. H. (2019). Geohazards in the three Gorges Reservoir Area, China–Lessons learned from decades of research. Engineering Geology, 261, 105267.

Van Genuchten, M. T. (1980). A closed-form equation for predicting the hydraulic conductivity of unsaturated soils. Soil science society of America journal, 44(5), 892-898.

Wang, B., Vardon, P. J., Hicks, M. A. (2018). Rainfall-induced slope collapse with coupled material point method. Engineering Geology, 239, 1-12.

Xu, H., He, X., Sheng, D. (2022). Rainfall-Induced Landslides from Initialization to Post-Failure Flows: Stochastic Analysis with Machine Learning. Mathematics, 10(23), 4426.

Yerro, A., Alonso, E. E., Pinyol, N. M. (2015). The material point method for unsaturated soils.

Géotechnique, 65(3), 201-217.

Yerro, A., Pinyol, N. M., Alonso, E. E. (2016). Internal progressive failure in deep-seated landslides. Rock Mechanics and Rock Engineering, 49(6), 2317-2332.

Yerro, A., Girardi, V., Martinelli, M., Ceccato, F. (2022). Modelling unsaturated soils with the Material Point Method. A discussion of the state-of-the-art. Geomechanics for Energy and the Environment, 100343.

Yerro, A., Soga, K., Bray, J. (2019). Runout evaluation of Oso landslide with the material point method. Canadian Geotechnical Journal, 56(9), 1304-1317.

Ying, C., Zhang, K., Wang, Z. N., Siddiqua, S., Makeen, G. M. H., Wang, L. (2021). Analysis of the run-out processes of the Xinlu Village landslide using the generalized interpolation material point method. Landslides, 18(4), 1519-1529.

Zhang, C., Yin, Y., Dai, Z., Huang, B., Zhang, Z., Jiang, X., ... Wang, L. (2021). Reactivation mechanism of a large-scale ancient landslide. Landslides, 18(1), 397-407.